2022 Project Abstract
For the Period Ending June 30, 2022

PROJECT TITLE: Develop Small and Inexpensive Purification System for Community Drinking Water
PROJECT MANAGER: Tianhong Cui
AFFILIATION: University of Minnesota
MAILING ADDRESS: 111 Church Street SE
CITY/STATE/ZIP: Minneapolis, MN, 55455
PHONE: 612-626-1636
E-MAIL: cuixx006@umn.edu
WEBSITE: https://cui.umn.edu/
FUNDING SOURCE: Environment and Natural Resources Trust Fund
LEGAL CITATION: M.L. 2018, Chp. 214, Art. 4, Sec. 02, Subd. 04e

APPROPRIATION AMOUNT: $425,000
AMOUNT SPENT: $425,000
AMOUNT REMAINING: $0

Sound bite of Project Outcomes and Results
This project designed a small water purification system for drinking water that can simultaneously remove the organic pollutants and heavy metal ions in the water. The system can be connected either to domestic drinking water taps or to water in lakes and rivers.

Overall Project Outcome and Results
This project is dedicated to providing clean drinking water to the Minnesota community by designing and manufacturing a small water purification system and providing a possible solution for the water treatment of large water plants. A compact size prototype was first designed to verify the mechanism. Photocatalysis technology was used to remove the organic pollutants, and titanium dioxide was selected as the photocatalyst. Electrochemical reduction was applied to remove heavy metal ions in the water. Finally, the team innovatively combined photocatalysis and electrochemistry to develop a photoelectrocatalytic solution that can simultaneously remove organic matter and heavy metal ions from water. The result shows that the compact system can remove 91.6% percent of the 10-micrometer methylene blue when the mass flow rate is 14.4 milliliters per hour (mL/h), and around 97.5% of 200 parts per million of copper(II) cations (Cu^{2+}) can be removed at the same time. After the theory of photoelectrocatalysis was verified, standard-sized systems were designed and fabricated comprising an ultraviolet lamp, a chamber with active carbon, and a microfluidic system with immobilized photocatalyst. The standard-size system can remove nearly 100% of the 10-micrometer methylene blue and 96% of the Cu^{2+} in the water with a flow rate of 50 mL/h. The team conducted the field test with the drinking water from Commonwealth Terrace Cooperative, a community for University of Minnesota students and their families, and the water from Mississippi River. The testing results demonstrate the capability of using the designed system to remove organic pollutants and heavy metal ions in the water.

Project Results Use and Dissemination
On-site demonstration and tests as described in the activities at a student housing community and Mississippi river from May through June 2022. Communications with interested entrepreneurs have been ongoing with interested parties including local companies and individuals.

The following papers published in archived journals and prestigious conferences:
1. Zhou, P., & Cui, T. (2020). Enhanced photocatalytic efficiency by layer-by-layer self-assembly of graphene and titanium dioxide on shrink thermoplastic film. Microsystem Technologies, 26(12), 3793-3798.
2. Zhou, P., Zhang, T., Simon, T. W., & Cui, T. (2021). Simulation and Experiments on a Valveless Micropump With Fluidic Diodes Based on Topology Optimization. Journal of Microelectromechanical Systems, 31(2), 292-297.

3. Zhang, T., Zhou, P., Simon, T., & Cui, T. (2022). Vibrating an air bubble to enhance mass transfer for an ultra-sensitive electrochemical sensor. Sensors and Actuators B: Chemical, 354, 131218.

Professor Tianhong Cui presented five invited public seminars and talks on water sensors:
Invited Talk, University of Bath, July 4, 2022
Invited Talk, University of Cambridge, July 11, 2022
Invited Talk, EcoLab, May 4, 2022
Invited Talk, French-American Innovation Days, Water Management in Cities, April 8, 2021 (on-line)
Invited Talk, University of Texas at San Antonio, September 13, 2019

Environment and Natural Resources Trust Fund (ENRTF)
M.L. 2018 FINAL REPORT

Date of Report: August 15, 2022

Date of Work Plan Approval: 06/05/2018

Project Completion Date: June 30, 2022

PROJECT TITLE: Develop Small and Inexpensive Purification System for Community Drinking Water

Project Manager: Tianhong Cui

Organization: University of Minnesota

Mailing Address: 111 church Street S.E.

City/State/Zip Code: Minneapolis, MN 55455

Telephone Number: (612) 626-1636

Email Address: cuixx006@umn.edu

Web Address: https://cui.umn.edu/

Location: Minneapolis, MN

Total Project Budget: $425,000

Amount Spent: $425,000

Balance: $0

Legal Citation: M.L. 2018, Chp. 214, Art. 4, Sec. 02, Subd. 04e as extended by M.L. 2021, First Special Session, Chp. 6, Art. 6, Sec. 2, Subd. 18

Appropriation Language: $425,000 the second year is from the trust fund to the Board of Regents of the University of Minnesota to develop a small and inexpensive purification-technology system for community drinking-water facilities to remove toxic contaminants, make water safe to drink, and improve drinking-water quality. This appropriation is subject to Minnesota Statutes, section 116P.10. This appropriation is available until June 30, 2021, by which time the project must be completed and final products delivered.

M.L. 2021, First Special Session, Chp. 6, Art. 6, Sec. 2, Subd. 18 ENVIRONMENT AND NATURAL RESOURCES TRUST FUND; EXTENSIONS. [to June 30, 2022]

I. PROJECT TITLE: Develop Small and Inexpensive Purification System for Community Drinking Water

II. PROJECT STATEMENT:

The objective of this project is to develop a small cheap purification system for cleaner community drinking water, as show in Figure 1. Current drinking water purification systems for community water are usually large, expensive, and difficult to operate. The proposed community water purification system is very small and low-cost, but more efficient to remove organic and inorganic contaminants. The water purification system is composed of porous activated carbon, reverse osmosis film, columnar UV light source, and a roll of multilayer purification film. The multilayer purification film is made of an electrically conductive film, by self-assembly of graphene and titanium oxide nanoparticles on the surface of plastic. When water purification is in progress, a small biased potential is applied to the conductive film, and the UV light is turned on. Water flowing into the system will be pre-treated by the activated porous carbon and reserve osmosis film, and some microbes, organic matters, small particles, nitrate and phosphate are removed. Next, the pre-treated water enters the multilayer purification film, where microbes can be further deactivated by the UV light and the porous structures. Water soluble ions, such as lead, cadmium, etc. can be reduced electrochemically or absorbed by the electric field. Titanium oxide, as a photosensitive material, will have photochemical behavior under UV illumination, to detoxify some organic matters. Through the above process, much cleaner drinking water can be obtained very efficiently. This project is intended to develop small, cheap, but efficient purification system for cleaner community drinking water.

In the next phase of the research, we will closely work with state agencies, water pollutant researchers, and industry to develop an implementation plan for pollutants reduction of drinking water in heavy industrial or agricultural regions in Minnesota.

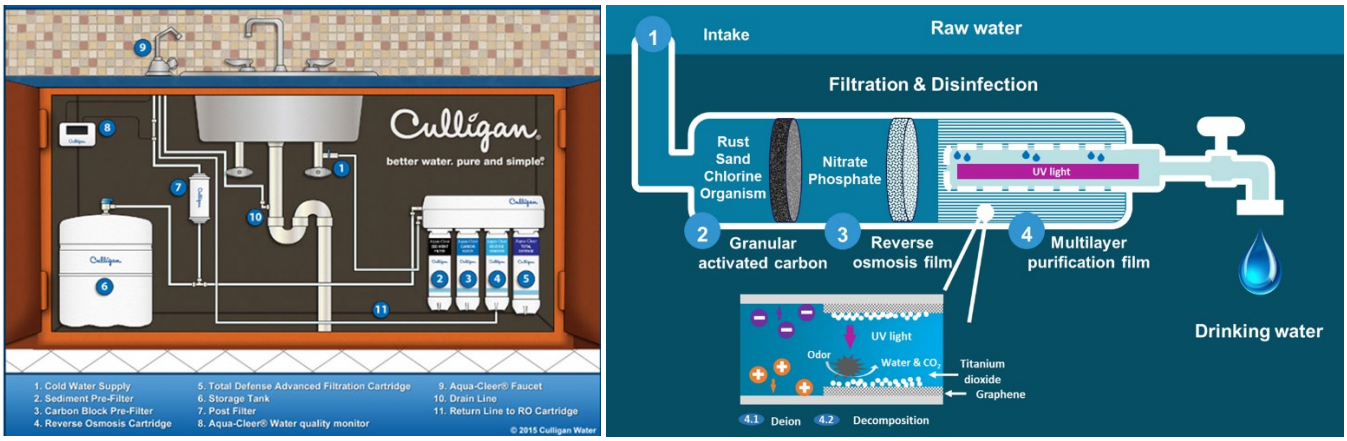

Current Technology **New Technology Proposed**

Figure 1. A comparison of drinking water purification system between the current and proposed technologies.

III. OVERALL PROJECT STATUS UPDATES:

First Update December 31, 2018:

The University of Minnesota team started this project on July 1, 2018. Professors Cui recruited one full-time research assistant conducting the work. Significant progress has been made. In this report are summaries of progress including the following sections: (1) Titanium dioxide with anatase crystal form was synthesized by sol-gel method and been used for photocatalytic water treatment. (2) Dispersion of titanium dioxide in water was also studied, and a feasible dispersion scheme was proposed. (3) The self-assembly method was used to immobilize titanium dioxide on glass substrate. (4) The structure and performance of the immobilized titanium dioxide thin film was tested by both atomic force microscope (AFM) and photodegradation of methylene blue. In summary, the initial 6-month work was successful.

Second Update June 30, 2019:

The University of Minnesota team made great progress from January 1, 2019 to June 30, 2019. Professors Cui, his full-time research assistant, and his part-time researcher have been conducting the research for this project. We investigated layer-by-layer self-assembly of titanium dioxide nanoparticles successfully. We studies different approaches to improve photocatalytic efficiency of titanium dioxide, including optimizing the number of deposition layers, synthesizing graphene-based titanium dioxide composite material, and using PMMA substrate with large surface area for water purification. We lined up resources and labs for the testing needs. In summary, the second 6-month work was productive and successful.

Third Update December 31, 2019:

The University of Minnesota team made great progress from July 1, 2019 to December 31, 2019. Professors Cui, his full-time research assistant, and his part-time researcher have been conducting the research for this project. We successfully synthesized graphene-based titanium dioxide composite material, and immobilized it on glass and polymer substrates using layer-by-layer self-assembly. We studied photocatalytic efficiency of the composite material, and compared with pure TiO_2. We also studied the effect of substrate materials, and the result indicates that immobilized composite material on shrink thermoplastic film has doubled photocatalytic efficiency than TiO_2 on a glass substrate. We also tested long-term stability of the immobilized composite material, and we observed no decrease of photocatalytic efficiency. In summary, the third 6-month work was productive and successful.

Fourth Update June 30, 2020:

The University of Minnesota team made steady progress from January 1, 2020 to June 30, 2020. Professors Cui, his full-time research assistant, and his part-time researcher have been conducting the research for this project. We successfully designed and fabricated microfluidic devices as a carrier of catalysis to further improve the mass transfer efficiency in the photocatalytic process and better achieve systematization. We used rGO/TiO_2 composite material as the photocatalyst, and the valveless micropump as an actuator of the system. We studied the performance of valveless micropump, and then evaluated water purification efficiency by photodegrading of methylene blue (MB). The result

shows that the system can remove 75% of the organics in water under the flow rate of 11 mL/h, and fully removal of the organics can be achieved under a lower flow rate. We will conduct detailed assessment in the next stage. In summary, the third 6-month work was progressive, even though the lab has been closed from March through June 2020 due to pandemic.

Fifth Update December 31, 2020:

The University of Minnesota team made steady progress from July 1, 2020 to December 31, 2020. Professors Cui, his full-time research assistant, and his part-time researcher have been conducting the research for this project. The full-size prototype was designed and fabricated in this stage. The core component of the water purification system is a microchannel array with photocatalyst coated. In addition, activated carbon was used to adsorb suspended solids and some organic pollutants in water. The performance of individual microchannel and a full-size prototype was evaluated by photodegrading of methylene blue (MB). The result shows that each microchannel can remove more than 90% of the organics in water under the flow rate of 14.4 mL/h, and full removal of the organics can be achieved under a lower flow rate of 3.6 mL/h. The full-scale model contains ten of the aforementioned microfluidic devices. Therefore, ten times the flow rate can be achieved without changing the degradation ratio. Due to pandemic, there is some delay in the research progress.

Project extended to June 30, 2022 by LCCMR 7/1/21 as a result of M.L. 2021, First Special Session, Chp. 6, Art. 6, Sec. 2, Subd. 18, legislative extension criteria being met.

Sixth Update June 30, 2021:

The University of Minnesota team made steady progress from January 1, 2021 to June 30, 202. Professors Cui, his part-time research assistant, and his part-time researcher have been conducting the research for this project. The main work of this stage is to add the function of removing heavy metal ions on the basis of the original system. The electrochemical reduction was first applied to remove heavy metal ions in the water, and the heavy metal ions removal was first considered as an individual module for the system. Cu2+ was considered as an example of heavy metal ions. The designed module can achieve 97.5% removal of 20 ppm Cu2+ ions in the water with a throughput of 2.5 ml/h. The Cu2+ concentration after purification was lower than the EPA standard for drinking water. Then the heavy metal reduction module was integrated with the photocatalyst organics removal module to simultaneously remove organic pollutants and heavy metal ions. The result shows the consistent performance of heavy metal reduction, and 25% enhanced organic removal efficiency. Due to pandemic, there is some delay in the research progress.

Seventh Update December 31, 2021:

The University of Minnesota team made steady progress from July 1, 2021 to December 31, 2021. Professors Cui, his part-time research assistant, and his part-time researcher have been conducting the research for this project. The main work of this stage is to further enhance the water purification efficiency by integrating the photocatalytic organics removal and heavy metal ions reduction into microfluidic devices. The influence of the microfluidic device was obtained by photocatalytic degradation of methylene blue in micro-channels with different thicknesses. The results show that the thinner the microfluidic channel has the higher the photocatalytic efficiency. Among them, a micro-channel with a thickness of 80 μm can degrade around 90% of methylene blue in one cycle, while the

photocatalyst in a 200 µm micro-channel can only degrade 60.4% of methylene blue with the same mass flow rate. Then the mass transfer efficiency was further improved by introducing air bubbles and vibration in the microchannel. Experiments have proved that with the help of the vibrating bubble, more than 97% of methylene blue can be degraded in one cycle. Due to pandemic, there is some delay in the research progress.

Overall Project Outcomes and Results as of June 30, 2022

This project is developed to provide clean drinking water to the Minnesota community by designing and manufacturing a small water purification system, a possible solution for the water treatment of large water plants. The University of Minnesota team completed the project successfully by June 30, 2022. Professors Cui, worked with one full-time research assistant, and one post-doc conducting the research. The team finished the proposed research in the proposed activities. A compact size prototype was first designed to verify the working mechanism. The photocatalysis technology was used to remove the organic pollutants, and the titanium dioxide was selected as the photocatalyst. Then the electrochemical reduction was applied to remove the heavy metal ions in the water. Finally, the team combined photocatalysis and electrochemistry to develop a photoelectrocatalytic solution that can simultaneously remove organic matters and heavy metal ions from drinking water. The result shows that the compact system can remove 91.6% percent of the 10 µM methylene blue when the mass flow rate is 14.4 mL/h, and the around 97.5% of 200 ppm Cu2+ can be removed at the same time. After the theory of photoelectrocatalysis was verified, standard-sized systems were designed and fabricated. The system consists of a UV lamp, a chamber with active carbon, and a microfluidic system with immobilized photocatalyst. The standard-sized system can remove nearly 100% of the 10 µM methylene blue and 96% of the Cu2+ in the water with a flow rate of 50 mL/h. The team conducted the field test with the drinking water from Commonwealth Terrace Cooperative, a community for University of Minnesota students and their families, and the water from Mississippi River. The testing results demonstrate the capability of using designed system to remove organic pollutants and heavy metal ions in the water.

Amendment Request as of 10/31/22

We are requesting funds be shifted from the travel and scientific services budget line to personnel.

- Travel budget would be reduced by $8,250 to a revised budget of $0
- Scientific services budget would be reduced by $63,764.62 to a revised budget of $26,235.38
- Personnel budget would increase by $44,599.49 to a revised budget of $348,730.49
- Equipment and supplies budget would increase by $415.13 to a revised budget of $50,034.13

These changes are being requested because more staff time was needed to accomplish Activity 2.

Amendment approved by LCCMR 12/16/22

IV. PROJECT ACTIVITIES AND OUTCOMES:

ACTIVITY 1: Development of small cheap community water purification systems

Description: The objective of this activity is to develop water purification systems using plastic, graphene and titanium oxide nanoparticles. The system is very small, cheap, and reliable to remove organic and inorganic contaminants in Minnesota community waters. The system will reduce the

water contaminants to meet the EPA and Minnesota standards, while the cost is one tenth and the room is one fifth of the traditional systems at most.

We propose a new drinking water purification system to be an alternative to conventional ones. We will develop new technologies enabling easy installation of smaller drinking water purification systems with very low cost and high efficiency. When water purification is in progress, a small biased potential is applied to the conductive plastic film, and the UV light is turned on. Water flowing into the system will be firstly pre-treated by the activated porous carbon and the reserve osmosis film, and some microbes, organic matters, small particles, nitrate and phosphate are removed. We will use a reverse osmosis film to remove nitrate and phosphate. Next, the pretreated water enters the multilayer purification film, where microbes can be further deactivated by the UV light and the porous structures. Water soluble ions, such as lead, cadmium, or nitrates, can be reduced electrochemically or absorbed by the electric field. Titanium oxide, as a photosensitive material, will have photochemical behavior under UV illumination, to detoxify some organic matters. Due to the outstanding material properties of graphene/ Titanium oxide and the advanced micromanufacturing techniques available at the University of Minnesota, we propose to make drinking water systems, which are small, cheap, and highly efficient. To meet the goal of the MPCA, this project will make significant impacts on drinking water purification in Minnesota waters.

Specific tasks will be:

1. Materials and hardwares development

Materials and hardwares are developed and demonstrated, which is expected to:
(1) Layer-by-layer self-assembled graphene/titanium dioxide nanocomposites.
(2) Hardwares for water purification systems.
(3) Initial testing results of water purification to remove organic and inorganic particles.

2. Development of drinking water purification systems

Drinking water purification systems are developed and demonstrated, which is expected to:
(1) Purification efficiency of small drinking water purification systems will be tested.
(2) Improved systems with optimized design, fabrication, and testing.
(3) Drinking water systems testing in Minnesota.
(4) Comprehensive assessment of the techniques.

Summary Budget Information for Activity 1:

ENRTF Budget:	**$ 275,569**
Amount Spent:	**$ 275,569**
Balance:	**$ 0**

Outcomes	Completion Date
1. Layer-by-layer self-assembly of graphene/titanium dioxide nanocomposites; hardware will be developed for water purification systems; Initial testing results of water purification to remove organic and inorganic particles	*6/30/2019*
2. Purification efficiency on small systems will be tested in comparison with conventional results in lab; Improved systems with optimized design, fabrication, and testing; Systems testing of water in Minnesota	*6/30/2020*

3. Comprehensive assessment of the techniques will be completed	*6/30/2020*

First Update December 31, 2018:

There are various methods for TiO_2 synthesis including sol-gel, liquid phase deposition, atomic layer deposition and self-assembly. The sol-gel is preferred because it can synthesize TiO_2 powder with simple equipment and process. The high chemical homogeneity in multi-component systems and doped systems makes it can be further used for the doping and surface modification process.

The synthesis process consists of two reactions: hydrolysis and condensation. The titanium isopropoxide is used as the precursor. The hydrolysis procedure of titanium isopropoxide produce titanium hydroxide, and the further condensation of titanium hydroxide produce titanium dioxide. The key point for this method is the hydrolysis speed. The high hydrolysis speed cause the agglomeration and coagulation, and large size TiO_2 particles can be expected. Too slow hydrolysis reaction extends the time for condensation from hours to days. The acetic acid is used as the chelating agent in the process as it can form the chelation with precursor and reduce the hydrolysis speed.

A series of experiments with different molar ratio of precursor to acetic acid were conducted to optimized the reaction speed and generate the best reactant ratio. The experiment results shows that the perfectly transparent sol can be generated when the molar ratio of precursor to acetic acid is 1:4, and it took 5 hours to transfer from sol to gel. The gel was dried in atmosphere pressure and 80°C for 24 hours and in vacuum for 1 hour. After that, the crystal was grind into powder and heated in furnace at 500°C for 2 hours. The multi-stage heating is required to evaporate the organic reactants and prevent the carbonization of organic components.

As the pre-processing for self-assembly, the dispersion of TiO_2 powders in water was also studied. The effect of pH was tested, and the particle size were also measured in different conditions. Based on the DLVO theory, when the pH is lower than isoelectric point pH, which is around 5 for the synthesized TiO_2 nanoparticles, the surface of the particle is positive charged, and the zeta potential is also positive. When the pH is higher than isoelectric point pH, the negative charged surface and zeta potential can be expected. However, the too low or too high pH value also means the high concentration of ionic, and the increasing ionic strength leads to the compression of the electrical double layer, and hence reduce zeta potential and increasing the aggregation of nanoparticles.

We obtained experiment results for particle size measurement under different pH value. The polyethylene glycol (PEG) with 400 molecular weight is used as the dispersant to cause steric repulsion between particles and help prevent the agglomeration. The ultrasonic treatment was also applied to reduce the particle size. The result shows that the smallest particle size can be expected when pH value is around 3 in acidic condition and 12 in alkaline condition. Thus, the 1 wt% TiO_2 water dispersion was prepared with both pH of 3 and 12.

Layer-by-layer self-assembly was used to immobilize TiO_2 nanoparticles on glass substrate. The 18mm × 18mm cover glass was used as the substrate. The glass was first treated by piranha solution for surface cleaning and hydroxylation. The surface of the pretreated glass was negative charged. Then the glass was immersed into the PDDA solution, which is positive charged, to generate the first layer thin film of PDDA, and the surface of the glass was now positive charged. For the TiO_2 water dispersion with pH=12, and the surface of the TiO_2 nanoparticles is negative changed, so the glass can be immersed into the solution directly to form a layer of TiO_2 thin film. The glass can be immersed in the PDDA and TiO_2 solution alternatively to generate multi-layer thin films. When the TiO_2 water dispersion with pH=3 was used, the surface of nanoparticles is positive charged, so that the PSS solution, which is negative changed, need to be used as the intermediate. The alternative deposition of PSS and acidic TiO_2 solution can also build multi-layer thin films.

The structure and features of the immobilized $\mathrm{TiO_2}$ thin film was characterized by AFM. It can be found that the surface area is increased by 7% compared to the original glass surface, and the higher surface area means the more location for photodegradation reaction and higher photocatalytic efficiency.

The photocatalytic efficiency was also been tested by photodegradation of organic compounds. The methylene blue was used for such experiment as photodegradation procedure of methylene blue can be tracked by the color change. It was found that 3 ml 100nmol/L methylene blue can be degraded by the immobilized $\mathrm{TiO_2}$ thin film on a 18mm $\times$ 18mm cover glass in 10 hours.

Second Update June 30, 2019

The previous work has been successfully prepared titanium dioxide (TiO_2) water dispersion, and the layer-by-layer self-assembly method was used to immobilize TiO_2 nanoparticles. The performance of the immobilized PSS/ TiO_2 composite material was tested by photodegradation of methylene blue, and the relatively low photocatalytic efficiency can be observed. Therefore, work in this stage focused on improving the photocatalytic efficiency of TiO_2.

The efficiency of photocatalysts is largely affected by the speed of generation and recombination of photoexcited holes and electrons. Compared to pure anatase or rutile, TiO2 consists of a mixture of these two crystal structures, showing higher photoreactivity because of the synergetic effect. Due to the difference of energy level of anatase and rutile, the photoexcited electrons can migrate to the conduction band of anatase, and the holes remain in the rutile. Therefore, the recombination is suppressed and the photoreactivity is increased. Thus, the commercial product Degussa P25, which consist of a mixture of anatase and rutile in a ratio of 79:21, is used as the photocatalysts for the following experiment.

Another effective way to increase photocatalytic efficiency is the graphene-based titanium dioxide. Graphene is an atomic sheet of sp2-bonded carbon atoms arranged into a honeycomb structure. The graphene/ TiO_2 composite material for water treatment has been studied in the last decades. It is believed that graphene can help increasing the photocatalytic efficiency in three ways: better adsorption of organics from water into the surface of TiO_2 due to the nature of carbon material, lower rate of electrons and holes recombination as it can transport the electrons, and achieve visible light photocatalytic possibly because of the low band gap of graphene/ TiO_2 composite material. The existing graphene based TiO_2 preparation methods are mainly chemical methods, requiring complex reaction processes as well as various chemicals and equipment. As the surface of graphene-based materials are negatively charged, the layer-by-layer self-assembly method can be applied to fabricate graphene-based TiO_2.

The immobilized $\mathrm{TiO_2}$ thin film was prepared using layer-by-layer self-assembly method. The surface hydroxylation treated cover glass is used as the substrate, and then the $\mathrm{TiO_2}$ thin film was deposited with a sequence of $[\mathrm{PDDA} + \mathrm{PSS} + \mathrm{PDDA}] + [\mathrm{PSS} + \mathrm{TiO_2}]_x$. The substrate was immersed into each solution for 10 min and rinse with DI water, then it was immersed into the next solution. The number of PSS/ $\mathrm{TiO_2}$ bilayers can be changed by alternative deposition of PSS and $\mathrm{TiO_2}$ on the substrate.

The effect of the number of PSS/ $\mathrm{TiO_2}$ bilayers was first studied. Different numbers of PSS/ $\mathrm{TiO_2}$ bilayers was deposited in glasses. The photocatalytic efficiency was evaluated by photodegradation of 100 μM methylene blue solution. The glass sample was placed in the glass tube filling with 6 mL methylene blue solution. The tube was first placed in dark for 1 h to reach a state of adsorption-desorption balance. Then the tube was radiated by a 15W 365nm UV lamp (XX-15L, Analytik Jena US LLC) for 5 h. 100μL solution was taken out every hour and the concentration of methylene blue was

measured by UV/VIS spectrometer. It can be inferred from the figure that the amount of methylene blue absorbed on the surface of TiO_2 in dark increases as the number of layers increases. The reason is that the amount of TiO_2 immobilized on the substrate is more when the number of layers is bigger, and the surface area of TiO_2 is also higher. Different from the continuous increasing of absorption, the photodegradation speed has a peak value when the number of bilayers is 5. This is because of the transparency change of the glass. With the increasing of PSS/ TiO_2 bilayers, the transparent of the glass decrease. When the number of bilayers is larger than 5 the glass is almost opaque, so the titanium dioxide on the back side of the glass is not exposed to ultraviolet light. Thus, the number of PSS/ TiO_2 bilayers has higher photodegradation efficiency and this value will be used as the reference to compare with the following experiments.

The photocatalytic efficiency of graphene-based TiO_2 composite material was also tested. As the amount of negative charged functional group on graphene is relatively small, it can only attract small amount of TiO_2 nanoparticles. In order to get a composite material with more TiO_2 nanoparticles, graphene oxide (GO) was used as there are more functional groups on graphene oxide. The GO/ TiO_2 composite material is fabricated by layer-by-layer self-assembly method in a sequence of $[PDDA + PSS + PDDA] + [PSS + TiO_2]_x + [GO + TiO_2]_y$. The total number of TiO_2 layers is 5, based on previous experiment, and the number of GO layers was changed from 0 to 5. When the number is 0 which means there is no GO/ TiO_2 but all PSS/ TiO_2 bilayers. It is as same as the reference condition. It can be found that the absorption in dark is less when there is GO/ TiO_2 bilayer exist. It is because that even though GO has more functional group than graphene, but it is still not comparable with the PSS, so the amount of TiO_2 nanoparticles is less in GO/ TiO_2 bilayers. However, the photodegradation speed of GO/ TiO_2 composite material is faster than pure PSS/ TiO_2 composite material although the amount of TiO_2 is less in GO/ TiO_2 composite material. The highest photodegradation efficiency occur when the number of GO/ TiO_2 bilayers is 3, and the efficiency is 56% higher than the reference group. The hypothesis of this phenomenon is that there is a tradeoff between the amount of GO and TiO_2, and it reaches a balance when there is 2 layers of PSS/ TiO_2 and 3 layers of GO/ TiO_2. More experiments will be designed to further explore this phenomenon and verify the hypothesis.

As a substitute for glass, PMMA film with large surface area was fabricated. The UV transparent PMMA film (0F058, Evonik Cyro LLC) can pass over 90% of ultraviolet light, which makes it possible to be used as substrate for photocatalytic water treatment. The hot embossing technique is used to increase the surface area of the material. The V shape Anodic Aluminum Oxide (AAO) is used as the mold. The diameter of the hole is 450 nm, and the depth is 1500 nm. The average height of the bulges is 678 nm, and the surface area is 3.14 times higher than flat surface. Next, the PMMA film will be used as the substrate of GO/ TiO_2 composite material, and the higher photocatalytic efficiency can be expected.

The PSS/TiO_2 and GO/ TiO_2 composite material was successfully fabricated by layer-by-layer self-assembly method. The number of bilayers was optimized by evaluating the photodegradation efficiency. The result shows that 5 bilayers lead to the best photodegradation performance. The performance of graphene based TiO_2 is also tested, and up to 56% enhancement of the photodegradation efficiency can be obtained by using GO/ TiO_2 composite material. The substrate of the TiO_2 will be changed from glass to PMMA film in the following experiments. The hot embossing of the PMMA film with AAO mold introduce nano-structures on the surface and therefore helps increasing the surface area 3.14 times higher.

Third Update December 31, 2019:

The previous work has been successfully immobilized TiO_2 and graphene oxide/TiO_2 (GO/TiO_2) composite material on glass substrate. Up to 56% enhancement of the photocatalytic efficiency was observed by using graphene-based material. The work in this stage wants to further enhance the efficiency by using different substrate material.

The glass was widely been used as the substrate for photocatalysis as it is ultraviolent transparent and cheap. However, glass substrate also brings some problems such as fragility and low specific surface area, and the photocatalytic efficiency is highly related to the amount of photocatalyst deposited in a physical area. Therefore, different substrate materials were used to increase the relative surface area of the photocatalyst and hence increase the photocatalytic efficiency. For example, the TiO_2 was deposited on glass spheres with a diameter of 5mm, and then put in a lab scale compound parabolic collector to photodegrade MB. Wang et al. successfully fabricated carbon nanotubes and TiO_2 composite films on cotton fabrics to achieve high photocatalytic efficiency. However, their irregular shapes and material properties make them hard to use when fabricating microfluidic systems or flexible structures.

In recent years, polymer-based devices have been considered to have great application potential due to some special properties of polymers such as low-cost, enhanced device performance, flexibility of the materials, and ease of fabrication. Thus, the polymer materials were considered as the substrate material. In order to increase the specific surface area, the surface modification of PMMA film and application of shrink thermoplastic film were two of the promising choices.

In previous work, the specific surface area of surface modification of PMMA film was increased by 3.14 times after hot embossing with Anodic Aluminum Oxide mold. On the other hand, shrink thermoplastic film can shrink more than 80% of its original size after heating, more than 5 times higher specific surface area can be expected. It has been successfully used in microsensors to enhance sensitivity and reduce the limit of detection, but it has never been used in photocatalytic water treatment.

The TiO_2 and GO/TiO_2 composite material was immobilized on glass and shrink thermoplastic material using layer-by-layer self-assembly method in a sequence of $[PDDA + PSS + PDDA] + [PSS/GO + TiO_2]_x$. Samples with different numbers of bilayers were prepared to optimize the performance. The size of film after shrinking was 18 cm by 18 cm which was the same as the cover glass. The coated shrink thermoplastic films were heated in the oven under 150 °C. Then the Ultraviolet light illumination was applied to reduce GO into rGO.

The structural and morphological properties of different photocatalysts on different substrates were investigated using scanning electron microscope (SEM) and atomic force microscope (AFM). It can be found that the PSS/TiO_2 bilayers on glass substrate were relatively flat, and the porous structure between photocatalysts was in nanoscale. The high-resolution images clearly show the TiO_2 nanoparticles. The size of TiO_2 nanoparticles were around 20-25 nm which matches with the particle size of P25. They also show that the surface of PSS/TiO_2 film on shrink thermoplastic film is rougher than rGO/TiO_2 film on shrink thermoplastic film, and it is because there is more TiO_2 immobilized on PSS than rGO as the negatively charged functional groups on rGO is much less than PSS.

The photocatalytic efficiency was evaluated by photodegradation of MB solutions. 10 mL MB with a concentration of 100 μM was used for photodegradation tests. Different numbers of PSS/TiO_2 bilayers on shrink polymer were first tested and compared. As shown in Figure 3a, concentration of MB kept decreasing with increasing illumination time. The concentration changes of MB slowed when its concentration was lower, which means that the kinetics of MB photodegradation can be described by the first order kinetics equation

$$\ln \ln (C/C_0) = -kt$$

where C and C_0 are the contaminant concentrations at the beginning and during light illumination, respectively, k is the reaction rate constant, and t is time. The photocatalytic efficiency can be represented by reaction rate constant k.

The same tests were also done with different numbers of PSS/TiO_2 bilayers on glass substrate and rGO/TiO_2 bilayers on shrink polymer substrate. It shows that the PSS/TiO_2 bilayers on glass substrate always have the lowest photocatalytic efficiency, and the highest photocatalytic efficiency observed was $k = 0.0106/\mathrm{min}$. The highest photocatalytic efficiency was obtained in shrink polymer with 6 rGO/TiO_2 bilayers. The highest reaction rate constant was $k = 0.0222/\mathrm{min}$, 2.1 times higher than PSS/TiO_2 bilayers on glass substrate and 1.28 times higher than PSS/TiO_2 bilayers on the shrink polymer substrate.

The cycling tests were also performed to show the long-term stability of LBL self-assembled rGO/TiO_2 bilayers on shrink polymer. A sample with 4 rGO/TiO_2 bilayers on shrink polymer was used for this test. 10 mL MB solution with 10 µM concentration was fully degraded within 1 h. It can be inferred from the figure that no decrease of photocatalytic efficiency was observed, which means that the bonding between photocatalyst and substrate is firm and the performance of photocatalyst is stable.

This study shows that the TiO_2 and rGO/TiO_2 can be firmly immobilized on glass and shrink thermoplastic film using LBL self-assembly method. The combined effect of folds structure induced by shrinking and the introduction of graphene material enhances the photocatalytic efficiency to 2.1 times higher than pure TiO_2 immobilized on glass substrate. Overall, more than 70% of 100 µM MB was removed in 1-hour using rGO/TiO_2 bilayers immobilized on shrink thermoplastic film, and the 10 µM MB can be fully removed within 1 hour. Next, the LBL self-assembly method will be performed in microfluidic device fabricated with polymer material. The photocatalytic efficiency will be further enhanced, and the model of proposed water purification system will be build based on microfluidic device.

Fourth Update June 30, 2020:

The MEMS technology was used to fabricate the microfluidic device that can be used for photocatalytic water purification. The microfluid device consists of two parts, a glass slide with photocatalyst and a polymer film with a microchannel structure. The glass slide was first covered by photoresist, and the photolithography was used to expose the window for photocatalyst. Then the rGO/TiO_2 composite material was coated on a glass slide using LBL self-assembly method, and the lift-off of photoresist helped to remove the photocatalyst outside the reaction chamber. The microchannel was first fabricated on a silicon wafer with SU8 photoresist by photolithography. Then a PDMS mold was fabricated based on the silicon mold. UV curing glue was applied between the PDMS mold and the organic film to build the micro-channel. The PDMS mold was removed before the UV curing glue was fully cured, and then the polymer film with microchannel and the glass slide with photocatalyst were attached. The microfluidic device for photocatalytic water purification can be obtained by fully curing the UV curing glue. A piezoelectric ceramic disk (lead zirconate titanate, PZT) was attached to the polymer film as an actuator.

The 10 µM MB solution was pumped through the microchannel to evaluate the photocatalytic efficiency. The mass flow rate was controlled by the voltage applied on PZT disk. It is clear that the mass flow rate increases as the voltage applied to the PZT increases because of the larger displacement of the PZT disk. The maximum mass flow rate of 11 mL/h can be achieved when the voltage applied on PZT disk is 60 V. This is because the residence time of the solution in the reaction chamber is inversely proportional to the flow rate. Therefore, a faster flow rate leads to shorter reaction time and higher

output concentration. As a result, around 75% of the MB can be removed when the highest mass flow rate was used, and more than 95% of the MB can be removed when the mass flow rate was 2 mL/h.

The nozzle-diffuser type valveless micropump was used for the above experiments, while the fluidic diode was believed that can be used to replace the nozzle-diffuser to achieve higher energy efficiency. The two-dimensional fluidic diode was first obtained using topology optimization based on the Density Model with Darcy interpolation. The ratio of energy dissipation between backward and forward flows was set as the objective function for topology optimization. Different sizes of the computational domains were used to obtain fluidic diodes of different geometries. It can be seen that the backward flow is divided into several tributaries which then interact with one another at their confluence, which leads to more resistance in the backward flow than in the forward flow.

The simulation of valveless micropumps was conducted by CFD. The mass flow rate through the micropump with the fluidic diode in the inlet and outlet surfaces. The net mass flow rate was calculated as 35.1 μg/cycle. The same calculation was conducted for the nozzle-diffuser micropump with a similar structure and the mass flow rate was 29.4 μg/cycle. Finally, the pressure of the actuation chamber was calculated. The pressure in the fluidic diode micropump is significantly smaller than for the nozzle-diffuser micropump. The performance of each micropump was evaluated using the net mass flow rate provided by a mechanical power, calculated as the average value of the integral of the product of force and speed over each point on the piezoelectric actuator total area over one cycle. The results show that the optimized fluidic diode micropump gives 27 times the pumping efficiency of the nozzle-diffuser micropump.

We verified the feasibility of graphene-based titanium dioxide as a photocatalyst for water treatment. We also verified the design of the reaction system based on microfluidic devices. The test result shows the correlation between the mass flow rate and the outlet pollutant concentration. We used rGO/TiO2 composite material as the photocatalyst, and the valveless micropump as an actuator of the system. We studied the performance of valveless micropump, and then evaluated water purification efficiency by photodegrading of methylene blue (MB). The result shows that the system can remove 75% of the organics in water under the flow rate of 11 mL/h, and fully removal of the organics can be achieved under a lower flow rate. We will conduct detailed assessment in the next stage.

Fifth Update December 31, 2020:

Purification efficiency on a small system was tested. Improved systems with optimized design, fabrication, and testing was also conducted. 10 μM methylene blue (MB) solution was flowed through the microchannel to evaluate the photocatalytic efficiency. The height difference between the inlet and outlet reservoir was adjusted for different mass flow rates. The concentration of the MB solution was measured by a spectrophotometer. It can be found that the removal ratio of the MB was inversely proportional to the mass flow rate. 91.6% percent of the MB was degraded when the mass flow rate is 14.4 mL/h. The MB degradation ratio increases with the increase of residence time. This is because a longer residence time means more chemical reaction time, making the degradation more thorough. At the same time, it can also be found that with the increase of residence time, the increase of MB degradation ratio becomes slow. This is because when the concentration of the reactant is too low, the mass transfer becomes a restrictive factor of the chemical reaction rate. At this time, more reaction time is required to degrade the same amount of organic matter. Although micro-channels have high mass transfer characteristics, for photocatalytic reactions with low concentrations, more effective mixing based on micro-channels, including passive mixing and active mixing, will be verified in subsequent improvements.

Sixth Update June 30, 2021:

Previous work has designed a full-size prototype of the photocatalytic water purification system. Organic pollutants in water can be effectively removed by photocatalytic technology, while the heavy metal removal mainly depended on the adsorption of activated carbon. Taking into account the increasingly serious heavy metal pollution and relatively inefficient activated carbon adsorption, the electrochemical reduction was integrated into the new system because of its higher heavy metal ions removal efficiency. In order to effectively remove heavy metal ions in the water body, in addition to the activated carbon adsorption in the pretreatment, we have introduced electrochemical reduction, a more efficient heavy metal ion removal technology. The traditional three electrodes system was applied, and a negative potential, which is lower than the redox potential of heavy metal ions, was applied on the working electrode. The heavy metal ions will be reduced to heavy metal elements when flowing through the working electrode, and the reduced heavy metal elements will be immobilized on the working electrode.

The microfluidic system was also integrated with electrochemical heavy metal removal because of its higher mass transfer rate. By replacing the counter electrode in electrochemical reduction with a photocatalyst, it is possible to simultaneously remove organic pollutants and heavy metal ions. The electrons generated by photocatalysis are transmitted to the working electrode to reduce heavy metal ions, which further promotes the separation of electrons and holes in the photocatalyst and improves the efficiency of photocatalysis.

The device was fabricated with PMMA to achieve low-cost fabrication. The copper foil was used as a working electrode because of its good adhesion with reduced heavy metal elements. The carbon paste was used as a counter electrode in the early stage of the experiment, and then it was replaced by rGO/〖TiO〗_2 composite material to achieve simultaneous removal of organic pollutants and heavy metal ions. The commercial Ag/AgCl electrode was used as a reference electrode.

Instead of using the planar reaction chamber as the previous work, a long microchannel was designed to achieve longer resident time and higher mass transfer rate. The total length of the microchannel is 60cm, which leads to around 60s residence time when the mass flow rate is 14.4 mL/h. The width of the microchannel is 1mm, and the height is 200 μm.

The Cu2+ ion was used as an example of heavy metal ions. Solution with 200 ppm Cu2+ was flowed through the microchannel to evaluate the performance of the heavy metal removal module. -0.8 V bias potential was applied on the working electrode to reduce the Cu2+ ions. The concentration of Cu2+ at the outlet was measured by a spectrophotometer with help of sodium diethyldithiocarbamate as it can form a yellow complex with Cu2+.It shows a significant enhancement of the Cu2+ removal after a long time operation. It was because the surface area of the working electrode was increased after immobilization of reduced Cu2+, and the number of active sites for reduction was also increased. It can be found that the concentration of Cu2+ at the outlet is lower than Environmental Protection Agency (EPA) standard after 3 hours of operation, and around 97.5% of Cu2+ was removed. Since the heavy metal adsorption on the working electrode is permanent and continuous, when the device is used next time, its removal efficiency will be further improved on the basis of 3-hour operation.

Then the counter electrode was replaced by rGO/TiO2 composite material. The testing was performed in bulk solution, and Methylene Blue (MB) was still used as an example of organic pollutants. The result shows the photocatalytic efficiency was enhanced by 25% when combine with the heavy metal removal module to form the photoelectrocatalysis. It is because the reduction reaction occurred at the working electrode and the electrons were transferred from the counter

electrode to the working electrode. Therefore, the photoexcited electrons were separated with holes and transferred to the working electrode. The prevented electron-hole recombination and longer lifetime of holes promote the oxidation of organics in counter electrode.

Seventh Update December 31, 2021:

N/A

Final Update June 30, 2022

The team developed a water purification system for the drinking water treatment. The system combined titanium dioxide based photocatalysis and electrochemical heavy metal ions reduction. The team successfully got initial testing results using glass-based compact microfluidic devices in lab. Methods including optimization of microchannel design and air bubble vibration were conducted to enhance the mass transfer as well as water purification efficiency. The methylene blue and Cu2+ were chosen as the example of organic pollutants and heavy metal ions. As a result, the compact system can remove 91.6% percent of the 10 µM methylene blue when the mass flow rate is 14.4 mL/h, and the about 97.5% of 200 ppm Cu2+ can be removed at the same time.

ACTIVITY 2: Development of standard size water purification systems and field testing

Description: A prototype standard size purification system to be assembled with the community water supply will be designed and constructed. We will develop prototype standard size purification system, as shown in Figure 2. The water purification system is composed of porous activated carbon, reverse osmosis film, columnar UV light source, and a roll of multilayer purification film.

Test sites will be set up to demonstrate the feasibility of the systems. Field testing will include picking up community sites and testing the efficiency of the systems in the field. Upon completion of the project, we will demonstrate the purification systems to the stakeholders, LCCMR committee members and officials.

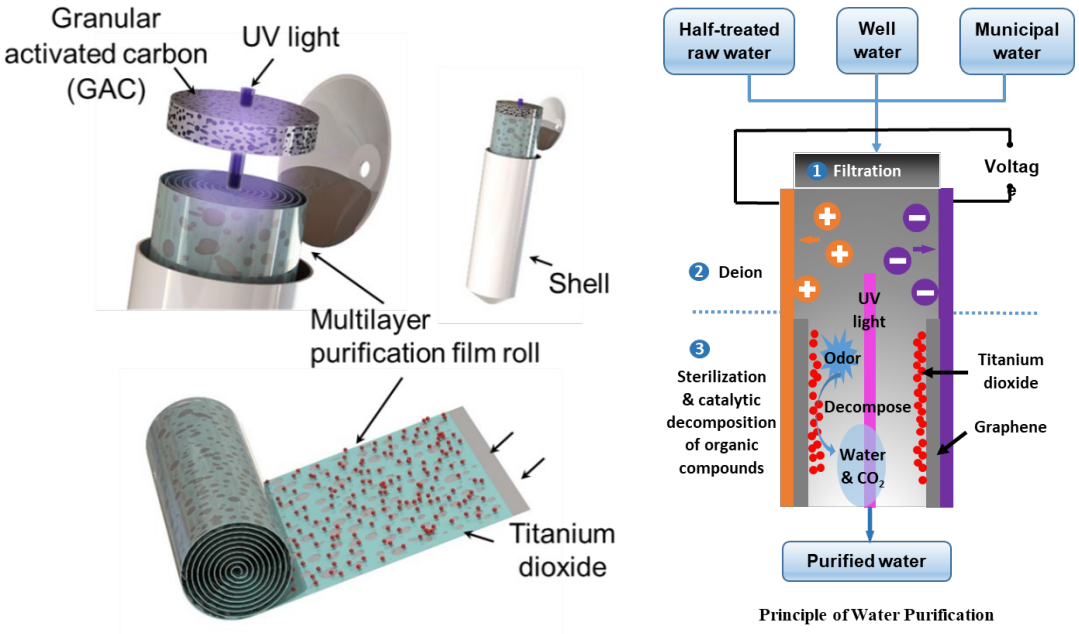

Principle of Water Purification

Figure 2. New Design of Drinking Water Purification System.

Specific tasks will be:

Development of standard size water purification systems and field testing

Standard size water purification systems and field testing are done, which is expected to:

(1) Designed and developed drinking water purification systems in standard size.
(2) Test sites with residential community water sites.
(3) Field testing at field sites, and tested purification efficiency.

Summary Budget Information for Activity 2:

ENRTF Budget: $ 149,431
Amount Spent: $ 149,431
Balance: $ 0

Outcomes	Completion Date
1. Standard size systems will be designed and developed	*12/31/2020*
2. One or two test sites with residential community water sites will be set up	*3/31/2022*
3. Field testing will be performed with filed sites, and purification efficiency will be tested	*6/30/2022*

First Update December 31, 2018:

N/A

Second Update June 30, 2019:

N/A

Third Update December 31, 2019:

N/A

Fourth Update June 30, 2020:

N/A

Fifth Update December 31, 2020:

Full-size prototypes of the photocatalytic water purification system have been fabricated. The testing based on an individual microfluidic device and the integrated system has shown relatively high photodegradation efficiency, and the feasibility of the design has also been verified. The only thing that is missing is that the fabrication of microchannels on large-sized flexible substrates is still in progress. It is believed that the flexible polymer-based microfluidic device will be deployed in the improved system as soon as possible, and the mass flow rate of the system will be further increased.

We fabricated a full-size prototype with a microchannel array. The model was fabricated by PMMA, and the inlet and outlet reservoirs were set at the upper and lower ends of the system, respectively. The water will flow through the activated carbon and the microchannel array in sequence.

Ten microfluidic devices were distributed around the ultraviolet lamp. The height difference between inlet and outlet reservoirs was 10cm, which leads to a mass flow rate of around 150 mL/h for the system, and 90.6% percent of the MB can be removed after the purification.

Due to the pandemic, there is some delay of the research progress. We applied for a no-cost extension for one more year to finish the overall project.

Sixth Update June 30, 2021:

In this stage of work, the heavy metal reduction module was added to the water purification system. The integration of heavy metal reduction and photocatalytic organic removal shows the high efficiency of simultaneous heavy metals and organic pollutants removal. A comprehensive assessment of the system will be completed, and some modification and optimization will be performed based on the testing result. The field test was delayed because of the COVID-19 pandemic and will be performed in the next stage. We plan to conduct the field tests during the 1-year extension.

Seventh Update December 31, 2021:

In this stage of work, the mass transfer efficiency was focused on to further improve the photocatalytic efficiency. Micro-channels and bubble vibration are introduced at the same time so that the photocatalytic efficiency is greatly improved, and finally, 97.5% of the organic matter can be removed in one flow.

The design of the microchannel with detailed structure of pockets for air bubble trapping was completed for enhancement of mass transport. The width of the microchannel is 1 mm, and the total length is 660 mm. In order to enhance the adhesion between photocatalyst and substrate, the glass slides used in previous work were replaced by Fluorine-doped Tin Oxide (FTO) glass. As a conductive metal oxide, the application of FTO makes it possible to combine the microfluidic device and photoelectrocatalysis system. All the other fabrication process was almost as same as previous work.

The photocatalysis performance in the microchannel was first studied without vibration. Different mass flow rate and different thickness of microchannel were compared. 10μM methylene blue flowed through the microchannel with solar light illumination, and the solution at the outlet is collected. The concentration of outlet methylene blue was measured by UV-Vis spectrometer. The microchannel 200 μm thick was first tested with different mass flow rates. It can be inferred from the result that the lower mass flow rate led to more degradation of methylene blue. This is due to the longer residence time of the solution in the microchannel at low flow rates, which also means more time for photocatalytic degradation. It can also be noticed that only 10% more methylene blue was degraded when the residence time is doubled. It is because the mass transfer rate is lower when the fluid flow is slower, and the total transmission mass is also limited at low concentrations. Experiments in a microchannel with 80 μm thickness confirmed this theory. It can be found that around 90% of the pollutants can be removed when flowing through the microchannel, which is 50% more than the microchannel 200 μm thick at the same mass flow rate. This result further illustrates the limitation of the mass transfer rate on the photocatalytic process, and the mass transfer rate is not high enough to rely on micro-channels alone.

The air bubble vibration was applied to further enhance the mass transfer. The air bubble was formed in the pocket structure shown because of the surface tension when the solution flows through. The PZT disk is used as the actuator for vibration. Microbeads 2 μm in diameter were used for particle image velocimetry (PIV). Different frequency was applied on the PZT disk and the flow field is characterized by the movement of the microbeads. The strongest circulation occurs at 8 KHz, the

resonance frequency of air bubbles, and the highest mass transfer coefficient can be expected. It can be found that 97.5% of the methylene blue can be removed with air bubble vibration. Although only 8.3% more methylene blue was removed compared to the case without air bubble vibration, the enhancement is still significant as the chemical reaction rate will become slower and slower as the concentration decreases. The impact of vibration intensity is studied by changing the voltage applied to the PZT disk. Not surprisingly, higher vibration intensity brings faster mass transfer efficiency, which further accelerates the photodegradation rate.

The field test was delayed because of the COVID-19 pandemic and will be performed in the next stage. We plan to conduct the field tests during the 1-year extension.

Final Update June 30, 2022

This project aims to design small and cheap water purification system for simultaneous removal of organic pollutants and heavy metal ions in drinking water. The standard-sized prototype was fabricated based on cheap polymer materials. Photoelectrocatalysis is the basic mechanism for organic and inorganic pollutants removal, and titanium dioxide was selected as the photocatalyst. The lab testing has shown compete organics removal and 96% removal of the heavy metal ions, and the field test also proved the performance of the system.

The microchannel was fabricated with the roll-to-roll technique. The structure of the microfluidic channel was first fabricated on double-sided tape by laser cutting. Then the two polymer sheets covered both sides of the tape to form the sealed microchannels. All operations are carried out on a roller 10 cm in diameter to reduce the internal stress after bending. The photocatalyst was deposited on the channel surface with layer-by-layer self-assembly technique, and half of the microchannels was covered with a thin layer of copper foil to serve as the electrode for electrochemical deposition. The standard-sized prototype consists of a UV lamp, a chamber with active carbon, and a microfluidic device with immobilized photocatalyst and copper foil.

The system was first tested in the lab with methylene blue and Cu2+ solutions. The efficiency of photodegradation and electrochemical reduction was evaluated separately. The number of TiO_2 layers and mass flow rate were two of the main factors that affect photodegradation efficiency. Different numbers of TiO_2 layers ranging from 1 to 9 were deposited in the microchannels, and the mass flow rate ranging from 10 mL/h to 50 mL/h was applied for the experiment. 10 μM methylene blue was still used as an example of the organic pollutants. The concentration of methylene blue in the outlet solution was measured by spectrophotometer. The result shows that more layers of TiO_2 always lead to more removal of methylene blue. Complete removal of methylene blue at 50 mL/h occurs when 9 layers of TiO_2 were deposited. The lower mass flow rate means a longer residence time of solution in the microchannels, and thus results in a higher removal rate with different number of TiO_2 layers. The complete removal of methylene blue can also be achieved with 7 layers of methylene blue and a mass flow rate of 20 mL/h.

The efficiency of heavy metal reduction was then studied by measuring the concentration of Cu2+ at the outlet. The deposition potential is the key factor for electrochemical deposition. It can be inferred from the result that lower deposition potential leads to a higher removal rate of Cu2+. It is because the lower deposition potential represents a larger potential difference and a higher chemical reaction constant. As a result, 96% of the Cu2+ can be removed from the water when the mass flow rate is 50 mL/h.

Finally, the performance of the standard-sized system was evaluated by the field test. The water samples from Commonwealth Terrace Cooperative, a community for University of Minnesota students and their families, and the Mississippi River were collected and used for testing. The

concentration of organic pollutants in the water samples before and after the purification was represented by the Chemical Oxygen Demand (COD), and the COD was measured with the colorimetric method. The performance of heavy metal reduction was evaluated by adding 1 ppm Cu2+ into the sample and measuring the removal rate of Cu2+ at the outlet. It can be found that the COD number was reduced to 67% and 82% for different samples, and the Cu2+ recovery rate was around 90% for both samples. Lower-than-expected organic removal may be due to the presence of refractory organics in the sample. Overall, the testing results demonstrate the capability of using the designed system to simultaneously remove organic pollutants and heavy metal ions in waters including drinking water and environmental water.

The field testing shows that the developed standard-sized system can simultaneously remove organics and heavy metal ions in the solution, and it's the first system that, to our knowledge, has this capability. The fabrication cost is mainly including the materials used and the PMDS mold for microchannel fabrication. Although the fabrication of the mold is relatively expensive, the mold can be used many times. Therefor the cost of a single system is around $20, which is much lower than existing water purification products. The low cost also makes it possible to scale up or pattern the system to overcome the problem of low throughput.

V. DISSEMINATION:

Description:

The findings will be disseminated through:

(1) On site demonstration as described in the activities
(2) Public seminars
(3) Progress update on www.me.umn.edu
(4) Presentations at national and international technical conferences
(5) Communications with interested entrepreneurs
(6) Peer reviewed papers
(7) Collaboration with MPCA

The technologies, if demonstrated successfully, may be implemented to community and home drinking water purification in the State of Minnesota and beyond. Any intellectual properties and related revenues as a result of the program will be shared between UMN and LCCMR.

First Update December 31, 2018:

N/A

Second Update June 30, 2019:

N/A

Third Update December 31, 2019:

N/A

Fourth Update June 30, 2020:

One peer reviewed journal paper was published in an archived journal in the following:
Zhou, P., & Cui, T. (2020). Enhanced photocatalytic efficiency by layer-by-layer self-assembly of graphene and titanium dioxide on shrink thermoplastic film. Microsystem Technologies.

Fifth Update December 31, 2020:

N/A

Sixth Update June 30, 2021:

Two research papers are under preparation for submission to academic journals.

Seventh Update December 31, 2021:

One peer reviewed journal paper was published in an archived journal in the following:
Zhou, P., Zhang, T., Simon, T. W., & Cui, T. (2021). Simulation and Experiments on a Valveless Micropump With Fluidic Diodes Based on Topology Optimization. Journal of Microelectromechanical Systems.

Final Update June 30, 2022
On-site demonstration and tests as described in the activities at a student housing community and Mississippi river from May through June 2022. Communications with interested entrepreneurs have been ongoing with interested parties including local companies and individuals.

The following papers published in archived journals and prestigious conferences:
1. Zhou, P., & Cui, T. (2020). Enhanced photocatalytic efficiency by layer-by-layer self-assembly of graphene and titanium dioxide on shrink thermoplastic film. Microsystem Technologies, 26(12), 3793-3798.
2. Zhou, P., Zhang, T., Simon, T. W., & Cui, T. (2021). Simulation and Experiments on a Valveless Micropump With Fluidic Diodes Based on Topology Optimization. Journal of Microelectromechanical Systems, 31(2), 292-297.
3. Zhang, T., Zhou, P., Simon, T., & Cui, T. (2022). Vibrating an air bubble to enhance mass transfer for an ultra-sensitive electrochemical sensor. Sensors and Actuators B: Chemical, 354, 131218.

Professor Tianhong Cui presented five invited public seminars and talks on water sensors:
Invited Talk, University of Bath, July 4, 2022
Invited Talk, University of Cambridge, July 11, 2022
Invited Talk, EcoLab, May 4, 2022
Invited Talk, French-American Innovation Days, Water Management in Cities, April 8, 2021 (on-line)
Invited Talk, University of Texas at San Antonio, September 13, 2019

VI. PROJECT BUDGET SUMMARY:

A. ENRTF Budget Overview: See attached budget spreadsheet

Explanation of Use of Classified Staff: N/A

Explanation of Capital Expenditures Greater Than $5,000: N/A

Number of Full-time Equivalents (FTE) Directly Funded with this ENRTF Appropriation: 1.11 FTE

Number of Full-time Equivalents (FTE) Estimated to Be Funded through Contracts with this ENRTF Appropriation: 0

B. Other Funds:

Source of Funds	$ Amount Proposed	$ Amount Spent	Use of Other Funds
State			
The university overhead unpaid	$205,087	$0	Develop a Small and Inexpensive Community Drinking Water Purification System
TOTAL OTHER FUNDS:	**$205,087**	**$0**	

VII. PROJECT STRATEGY:

A. Project Partners:

Tianhong Cui, Distinguished McKnight University Professor at the University of Minnesota, will serve as PI and project manager. Professor Cui is a leading expert on advanced manufacturing and micro devices. He will be responsible for overseeing the project, all reports, and deliverables. A research assistant and a post-doc will develop the systems, in-lab test sites with dirty water, and set-ups for field testing of the proposed purification systems for community drinking water.

B. Project Impact and Long-term Strategy:

Minnesota Pollution Control Agency (MPCA) works together with other agencies and advocacy groups in developing strategy to keep clean drinking water, reducing their impacts on human health and the environment. Water is one of the most valuable natural resources in the world. In everyday life, people use water in many ways, such as drinking, cooking, washing, etc. It is very important to ensure the supplied water is clean, especially the drinking water for daily life. Although tap water meeting federal and Minnesota state standards is usually safe to drink, people are still confronted with an increasing threat to contaminated water. It has been reported that over 200,000 violations to federal drinking water standards each year, among which more than 20% are due to poor water treatment facilities. Therefore, a small cheap but efficient community water purification system is very important to ensure a healthy drinking water supply, especially for those who are vulnerable to waterborne diseases. Commercially available community water treatment systems utilize various water cleaning technologies with several components, including activated carbon filter unit, ion exchange unit, reverse osmosis unit, and distillation unit. The purification system consists of a sediment pre-filter, a carbon block pre-filter, a reverse osmosis cartridge, and a total defense advanced filtration cartridge. Through the above units, contaminants, such as heavy metal ions, microbes, dissolved solids, organic pollutants can be removed from the water, so that clean drinking water can be obtained. The commercial systems provide the users with purified drinking water, but the price is relatively high, ranging from hundreds to thousands dollars. In addition, due to the large volume of the purification systems, it occupies much room. The proposed new purification system will provide a solution to current ineffective and expensive community water treatment systems, and thus ensure people's cleaner drinking water in Minnesota.

The knowledge learned throughout the project will provide a solid foundation for further research and development that would lead to eventual implementation of the new technique practically enabling broader treatment of Minnesota's water. This will provide a solution to current ineffective water treatment, ultimately help implement the MPCA's clean water strategy, and thus ensure people's safety in Minnesota.

In addition, we will plan to file patents on the proposed community drinking water purification system for commercialization in the future. We can also use the new technology for treatment of natural water, waste water, etc. As a result, the innovative technology can benefit the local residents and society by purifying the waters in Minnesota.

C. Funding History:

Funding Source and Use of Funds	Funding Timeframe	$ Amount
Mocon Inc., Graphene gas sensors	Nov. 2014 - July 2016	$173,199
Alexandria Extrusion Inc., Microstructures for Heat Transfer	Nov. 2011 - Dec. 2015	$165,516
DARPA, MEMS-Based Active Heat Sink Technology	Jan. 2009 - Sept. 2013	$2,579,025
MN Partnership, Nano-Sensors	Jan. 2010 – Dec. 2012	$637,500

VIII. FEE TITLE ACQUISITION/CONSERVATION EASEMENT/RESTORATION REQUIREMENTS:

IX. VISUAL COMPONENT or MAP(S):

X. RESEARCH ADDENDUM:

XI. REPORTING REQUIREMENTS:

- The project is for 4 years, will begin on 07/01/18, and end on 06/30/22.
- Periodic project status update reports will be submitted [06/30] and [12/31] of each year.
- A final report and associated products will be submitted between June 30 and August 15, 2022.

Appendix: Visual Component

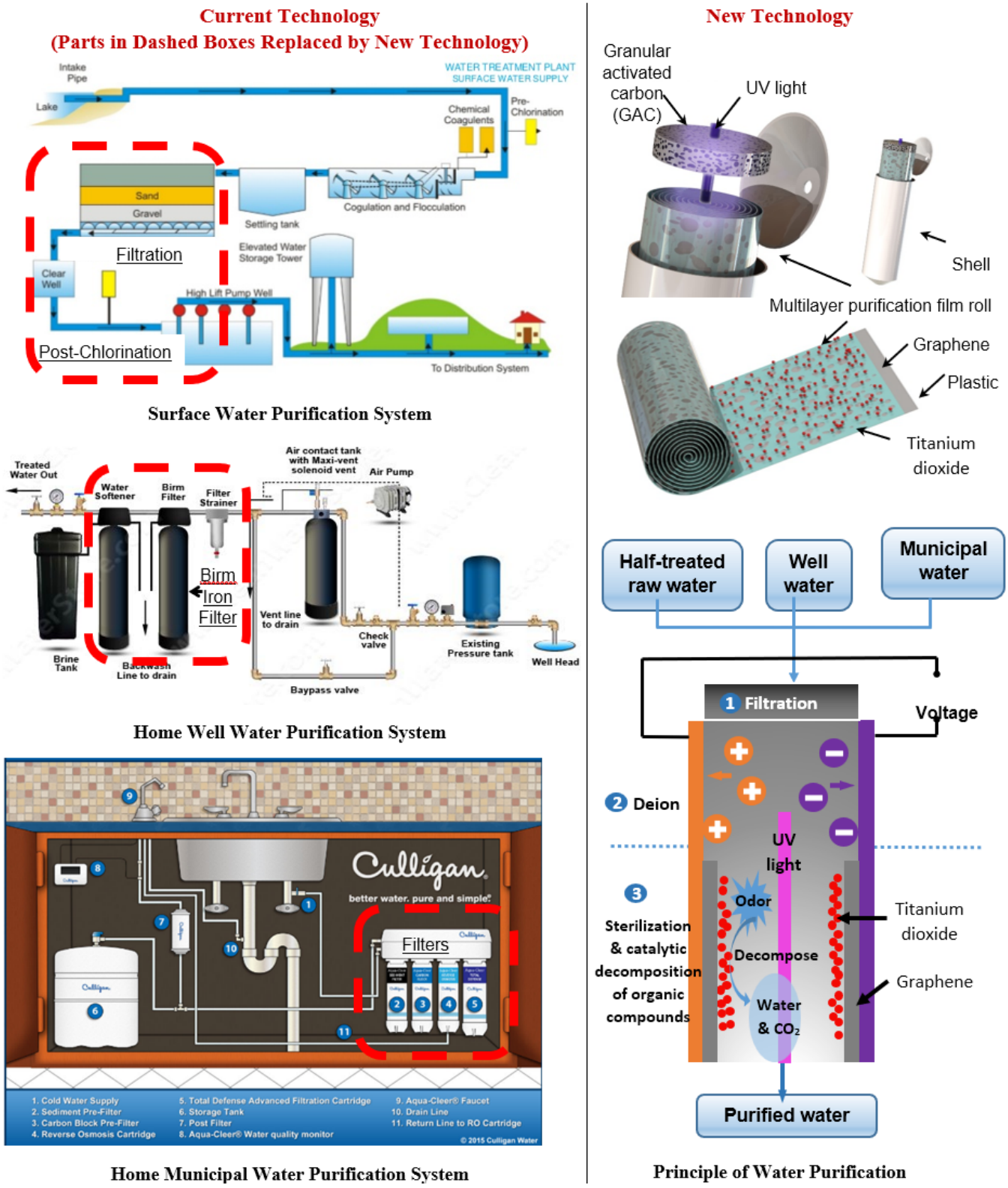

Figure 1: Design of the proposed water purification and comparison with existing technologies.

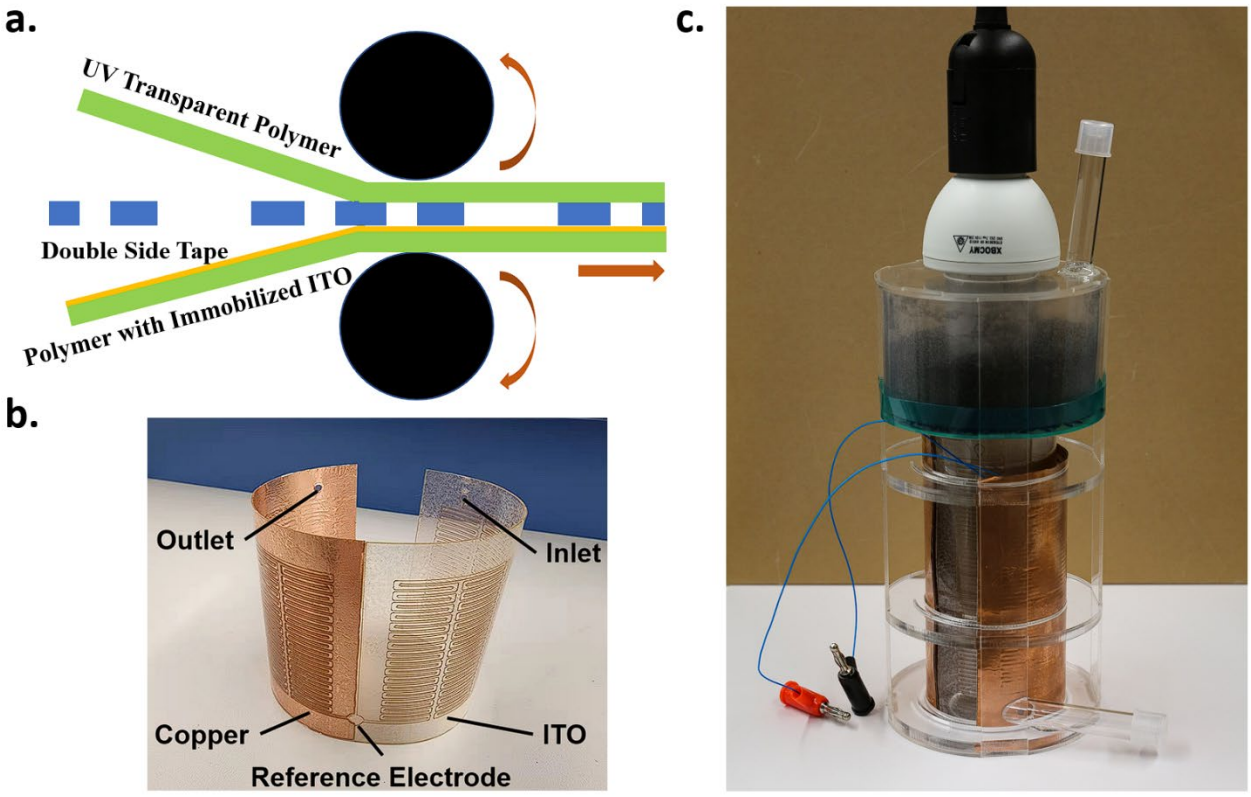

Figure 2: (a) Scheme of the polymer based microchannel fabrication (b) picture of fabricated microfluidic device based on polymer material (c) picture of standard size prototype for water purification.

Attachment A:
Environment and Natural Resources Trust Fund
M.L. 2018 Budget Spreadsheet - FINAL

Project Title: Develop Small and Inexpensive Purification System for Community Drinking Water
Legal Citation: ML 2018 ch214 Art4 Sec 2 Sub04e E8181PS
Project Manager: Dr. Tianhong Cui
Organization: University of Minnesota
College/Dept/Div: College of Science and Engineering, Dept of Mechanical Engineering
M.L. 2018 ENRTF Appropriation: $425,000
Project Length and Completion Date: 4 years/ June 30, 2022
Date of Report: Actuals 8/9/22

ENVIRONMENT AND NATURAL RESOURCES TRUST FUND BUDGET	Amended Budget	Amount Spent	Balance
BUDGET ITEM			
Personnel (Wages and Benefits) - overall	$348,730	$348,730	$0
Dr. Tianhong Cui, PI, 1 month summer salary (11% FTE) & 33.5% fringe for 3 years (Total estimated amount $69,512)			
Post-Doc or visiting scholar, 6 months (50% FTE) plus 21.4% fringe for 3 years Total estimated amount $90,056)			
Graduate Research Assistant, 50% FTE (fall & spring semesters include 16.9% fringe plus $18.94/hour tuition, summer 15% fringe only) for 3 years (Total estimated amount $144,563)			
Professional/Technical/Service Contracts			
Equipment/Tools/Supplies			
Lab Materials & Supplies: fabrication materials & supplies including polymer substrates ($10,000), nanomaterials and chemicals ($15,000), roll-to-roll manufacturing set-up items ($14,619), bottles, gloves, other electronics for testing, etc. ($10000)(Total estimated amount $49,619)	*$50,034*	*$50,034*	$0
Travel expenses in Minnesota			
Travel- Cui Domestic travels: Mileage, lodging, and meals for travel to and between the drinking water testing sites and the university based on the university compensation policy	*$0*	*$0*	$0
Other			
Scientific Services: User fees at Minnesota Nano Center and Characterization Facility at the University of Minnesota. The cost is estimated at about $1,000 per month for the Post-Doc, and $750 per month for the research assistant for 3 years. Actual charges based on equipment rate and time used will be charged. (See note below)	*$26,235*	*$26,235*	$0
COLUMN TOTAL	$425,000	$425,000	$0

Microsystem Technologies (2020) 26:3793–3798
https://doi.org/10.1007/s00542-020-04865-y

TECHNICAL PAPER

Enhanced photocatalytic efficiency by layer-by- layer self-assembly of graphene and titanium dioxide on shrink thermoplastic film

Peng Zhou[1] · Tianhong Cui[1]

Received: 20 April 2020 / Accepted: 28 April 2020 / Published online: 9 May 2020

Abstract
In this work, reduced graphene oxide/titanium dioxide (rGO/TiO_2) composite material was immobilized on shrink thermoplastic film using layer-by-layer (LBL) self-assembly to remove pollutants in water, and the results were compared with immobilized TiO_2 on glass and shrink thermoplastic film. The structural and morphological properties of the immobilized photocatalysts were investigated using atomic force microscope and scanning electron microscope. The photocatalytic efficiency was measured by photodegradation of methylene blue under solar light illumination. The immobilized rGO/TiO_2 on shrink thermoplastic film showed doubled photocatalytic efficiency than TiO_2 on glass substrate, and no decrease of photocatalytic efficiency was shown after 5 h of operation. The use of shrink thermoplastic film and the introduction of graphene material contribute to an increase in catalytic efficiency of 63% and 28%, respectively. These results lead us to believe that the LBL self-assembled rGO/TiO_2 composite on shrink thermoplastic film could be used in photocatalytic degradation of other water pollutants.

1 Introduction

Water shortage is becoming a global challenge. Access to clean water is a problem not only in developing countries, but also in developed countries including the United States because of economic growth, demographic shift and climate change. There are approximately four billion people facing water scarcity, and water pollution makes their situation even more severe. In fact, the United Nations lists addressing water scarcity and water pollution as one of the goal challenges for sustainable development by 2030 (Desa 2016).

Photocatalytic technology based on titanium dioxide (TiO_2) has gained wide attention in the past decades as a low-cost, environmentally friendly and sustainable water treatment technology. This technology uses semiconductor catalysts such as TiO_2 to mineralize refractory organic compounds, water pathogens and disinfection by-products (Pera-Titus et al. 2004). When TiO_2 is illuminated under photon energy greater than or equal to the bandgap energy of TiO_2, the distinct lone electron in the outer orbital is photoexcited to the empty conduction band, leaving a hole in the valence band. A series of redox reactions occur at the photo active surface and can remove the organics in water (Fujishima et al. 2008). However, low efficiency, catalyst agglomeration during operation, and the complex post-separation process are the primary barriers that prevent practical applications of this technology.

Graphene, a flat monolayer of sp^2-bonded carbon atoms, is believed to be very effective in increasing photocatalytic efficiency because of the enhanced charge transfer rate (Zhang et al. 2010). Many approaches have been applied to synthesize graphene-based TiO_2 photocatalysts. For example, Guo et al. (2011) used an ultrasonic assisted chemical reaction to synthesize rGO/TiO_2 composite material and observed 2.57 times enhanced photocatalytic efficiency. Safardoust-Hojaghan and Salavati-Niasari (2017) synthesized rGO/TiO_2 composite material using a hydrothermal method, and it showed 2.13 times faster photodegradation speed than TiO_2. All of these chemical methods require complex and expensive chemical reactions, and the final products are in powder form, which is difficult to be immobilized on the substrate.

As the slurry of TiO_2 and rGO/TiO_2 composite material requires a post-separation process and leads to catalyst agglomeration during operation, hindering the practical

✉ Tianhong Cui
cuixx006@umn.edu

[1] Department of Mechanical Engineering, University of Minnesota, Minneapolis, USA

application of this technology (De Lasa et al. 2005), some researchers tried to deposit photocatalysts on different substrates using chemical vapor deposition (Alotaibi et al. 2018), atomic layer deposition (Klesko et al. 2018) and, most commonly, the sol–gel method (Al-Mathloom and Abed 2019). However, all of these methods start with a titanium precursor and require complex chemical reactions. In addition, the enhancement of graphene-based TiO_2 in photocatalytic efficiency becomes limited when the composite material is immobilized on the surface of the substrate due to the reduction of active sites involved in the reaction. For example, Padoin et al. (2016) immobilized rGO/TiO_2 composite material on the walls of microchannels, and only 29% enhancement was observed compared to immobilized pure TiO_2.

Instead of using these chemical deposition methods, the physical LBL self-assembly is more convenient, and can produce a high-quality TiO_2 film on a substrate. The basic mechanism of LBL self-assembly is the electrostatic interaction between polymer or particles with opposite charges (De Villiers et al. 2011). Multilayered TiO_2 or rGO/TiO_2 films can be deposited onto an electrically charged substrate by dipping the substrate into alternating solutions with opposite charges. This deposition routine can be repeated many times to fabricate multilayer photocatalyst thin films. TiO_2/Polymer nanocomposite films has been successfully fabricated since 1997, when Liu et al. (1997) fabricated as many as 120 layers of films on silicon, metal and plastic substrates. Yao et al. (2010) fabricated a graphene-based TiO_2 photocatalysts on glass substrate in a sequence of GO/PDDA/TiO_2 while Manga et al. (2009) fabricated the material in a sequence of PEI/TiO_2/PEI/GO. Manga's group also used femtosecond transient absorption spectroscopy to demonstrate the ultrafast photocatalytic electron transfer between TiO_2 and graphene. Different substrate materials were used to increase the relative surface area of the photocatalyst, therefore increase the photocatalytic efficiency. For example, TiO_2 was deposited on glass spheres with a diameter of 5 mm, and then put in a lab scale compound parabolic collector to photodegrade methylene blue (MB) (Cunha et al. 2018). Wang et al. (2017) successfully fabricated carbon nanotubes and TiO_2 composite films on cotton fabrics to achieve high photocatalytic efficiency. However, their irregular shapes and material properties make them hard to use when fabricating microfluidic systems or flexible structures.

In this work, a shrink thermoplastic film was used as a substrate material as it can shrink more than 80% of its original size after heating. It has been successfully used in microsensors to enhance sensitivity and reduce the limit of detection (Li et al. 2015), but it has never been used in photocatalytic water treatment. TiO_2 films and rGO/TiO_2 composite films were LBL self-assembled on shrink polymer films, respectively. The photocatalytic efficiency was measured and compared with TiO_2 films on a glass substrate, and the morphological properties were measured to explain the difference.

2 Experimental

2.1 Materials

Poly(sodium 4-styrenesulfonate) (PSS; M_w = 70,000), Poly(diallyl dimethyl ammonium chloride) (PDDA; 20 wt% in water), and TiO_2 nanoparticle (P25, 30% rutile and 70% anatase phase) were obtained from Sigma-Aldrich, and monolayer graphene oxide water dispersion (4 mg/ml) was purchased from MSE Supplies LLC. Shrink thermoplastic films were acquired from Grafix Arts LLC.

2.2 LBL self-assembly process

The 1 wt% TiO_2 cationic solution was prepared by adding 1 g TiO_2 and 1 mL HCl (1 M) into 100 mL deionized water, followed by more than 24 h of continuous stirring until a stable colloid solution was formed. The GO solution was diluted to 1 mg/mL with deionized water, followed by slight sonication to prevent agglomeration. A shrink thermoplastic film was cut into 45 cm squares, and the 18 cm square glass was also used for comparison.

The schematic diagram of LBL self-assembly process is shown in Fig. 1. The substrates were first cleaned by deionized water and dried in air. Then the substrates were alternately immersed into cationic PDDA and anionic PSS solutions in a sequence of [PDDA + PSS + PDDA]. The long-chain polymers with charged branches helped to form a uniformly film on the substrates. Next, the PSS/TiO_2 bilayers or GO/TiO_2 bilayers were deposited on top of the substrates. Different numbers of composite photocatalyst bilayers were prepared. Deposition time for each process was 10 min, accompanied by the washing out of non-bound molecules after each layer was deposited.

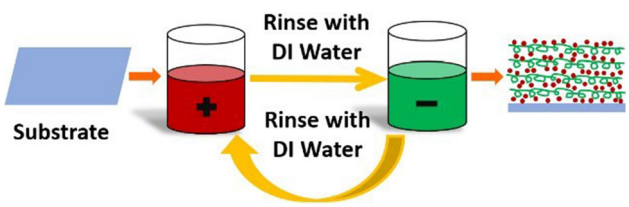

Fig. 1 Schematic diagram of LBL self-assembly process

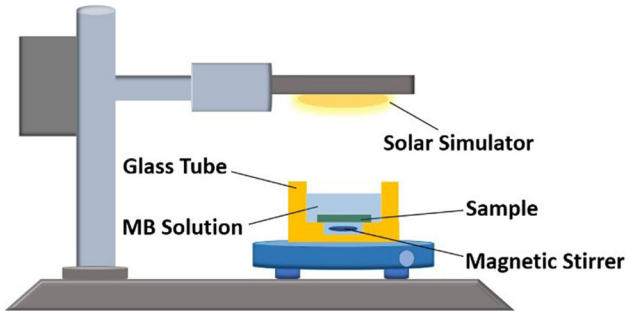

Fig. 2 Setup of the photocatalytic tests

The coated shrink thermoplastic films were heated in the oven under 150 °C. The film size after shrinking was 18 cm by 18 cm, the same as the cover glass. Then the Ultraviolet light illumination was applied to reduce GO into rGO (Williams et al. 2008).

2.3 Measurement and characterization

The surface morphologies and elemental mapping of samples were observed by a Field Emission Gun Scanning Electron Microscope (FEGSEM) (Hitachi SU8230). A thickness of 2.5 nm Iridium was deposited on each sample to increase the conductivity. The three-dimensional surface topography was measured by Atomic Force Microscopy (AFM) (MFP-3D Origin AFM, Asylum Research).

Photocatalytic efficiency of immobilized photocatalysts was evaluated by degrading MB. Figure 2 shows the setup of the photocatalytic experiments. The back of prepared samples was covered by waterproof tape, and the samples were placed in a customer designed glass tube with a volume of 12 mL. The magnetic stirrer was placed under the sample to increase the mass transfer from bulk solution to the surface of photocatalysts. 10 mL MB with a concentration of 100 μM was used for photodegradation tests, and 10 μM MB with the same volume was used for cycling tests. The tube was first placed in the dark for 1 h to reach the adsorption–desorption balance of MB from the photocatalysts. Then the tube was illuminated by solar light for 1 h. 100 μL solution was taken from the tube every 10 min, and the concentration of MB was measured by UV/Visible

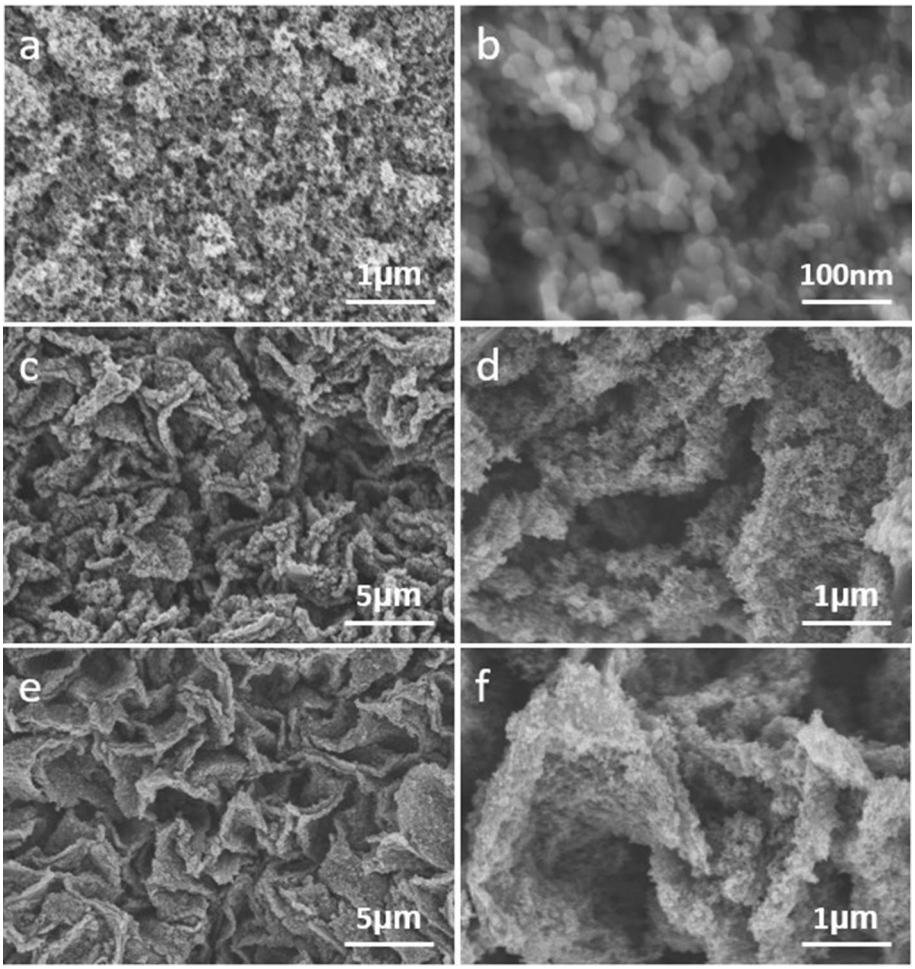

Fig. 3 SEM images of different photocatalyst in different substrate **a** 4 PSS/TiO_2 bilayers on glass substrate, high resolution, **b** 4 PSS/TiO_2 bilayers on glass substrate, ultra-high resolution, **c** 4 PSS/TiO_2 bilayers on shrink polymer, low resolution, **d** 4 PSS/TiO_2 bilayers on shrink polymer, high resolution, **e** 4 rGO/TiO_2 bilayers on shrink polymer, low resolution and **f** 4 rGO/TiO_2 bilayers on shrink polymer, high resolution

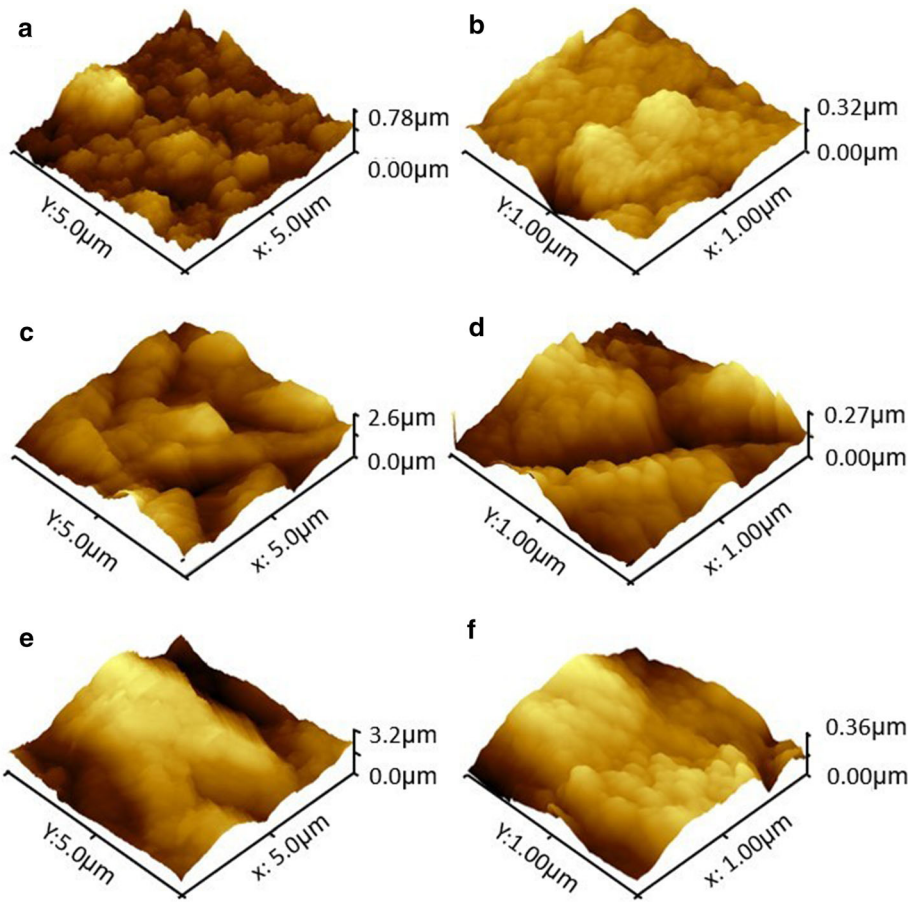

Fig. 4 AFM images of different photocatalyst in different substrate **a** 4 PSS/TiO_2 bilayers on glass substrate, low resolution, **b** 4 PSS/TiO_2 bilayers on glass substrate, high resolution, **c** 4 PSS/TiO_2 bilayers on shrink polymer, low resolution, **d** 4 PSS/TiO_2 bilayers on shrink polymer, high resolution, **e** 4 rGO/TiO_2 bilayers on shrink polymer, low resolution and **f** 4 rGO/TiO_2 bilayers on shrink polymer, high resolution

Spectrophotometer (Model SP-UV1100, DLAB Scientific Co., Ltd) under a wavelength of 664 nm.

3 Result and discussion

3.1 LBL self-assembly and characterization

The morphology of immobilized photocatalysts was observed by SEM. Figure 3 shows the SEM images of 4 PSS/TiO_2 bilayers on both a glass substrate and a shrink thermoplastic film and 4 rGO/TiO_2 bilayers on the shrink thermoplastic film. It can be found that the PSS/TiO_2 bilayers on glass substrate were relatively flat, and the porous structure between photocatalysts was in nanoscale. The ultra-high-resolution image of glass sample clearly shows the TiO_2 nanoparticles. The size of TiO_2 nanoparticles were about 20–25 nm which matches the particle size of P25. Comparing the photocatalysts on the glass substrate with the shrink thermoplastic films, Fig. 3c, e show many folds produced by shrinking, which means a higher surface area can be expected on shrink thermoplastic films. It also leads to the microscale porous structures on the substrate. The amount of folds was similar between PSS/TiO_2 and rGO/TiO_2 composite films on shrink thermoplastic films, but Fig. 3c, d show the surface of the folds was rougher than Fig. 3e, f. This is because there is more TiO_2 immobilized on PSS than rGO as the negatively charged functional groups on rGO is much less than PSS.

Figure 4 shows the AFM images of different photocatalysts on different substrates. Similar to the SEM images, the photocatalysts on a glass substrate were smoother than that on a shrink polymer substrate. In a square with a side of 5 μm, the height difference of photocatalysts on the glass substrate was 783 nm, while the value on the shrink polymer substrate with different photocatalysts were 2.644 μm and 3.315 μm, respectively. The microscale folds on the shrink polymer were also visible in AFM images. The particle size shown in high resolution images were in a range from 20 to 25 nm, which matches the SEM results.

3.2 Photocatalytic tests and efficiency

The photocatalytic efficiency was evaluated by photodegradation of MB solutions. Different numbers of PSS/

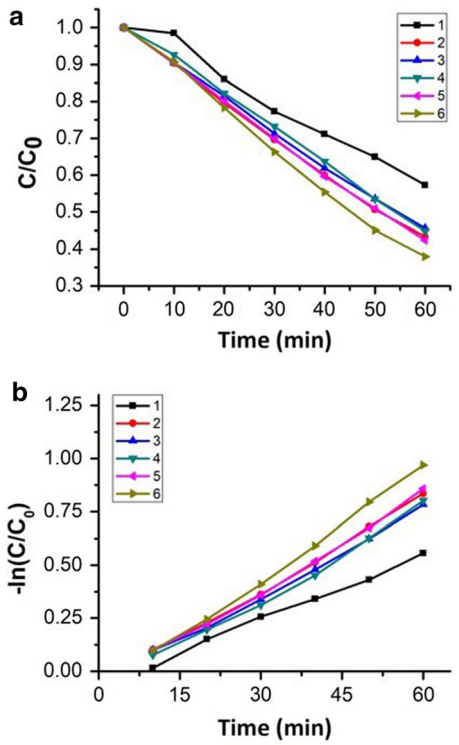

Fig. 5 **a** Relative MB concentration versus irradiation time with different numbers of PSS/TiO_2 bilayers and **b** MB degradation kinetics for different numbers of PSS/TiO_2 bilayers

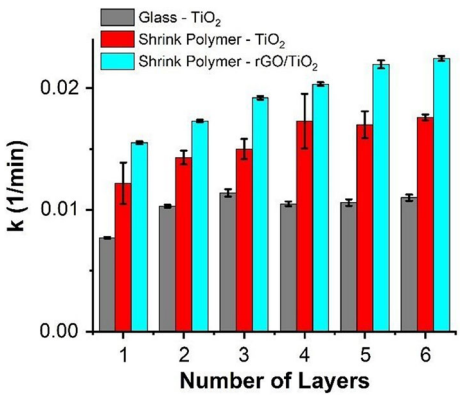

Fig. 6 Pseudo first order kinetic constant for different number of PSS/TiO_2 and rGO/TiO_2 bilayers on different substrate

TiO_2 bilayers on shrink polymer films were first tested and compared. As shown in Fig. 5a, concentration of MB kept decreasing with increasing illumination time. The concentration change of MB slowed down when its concentration was lower, thus the kinetics of MB photodegradation can be described by the first order kinetics equation

$$ln(C/C_0) = -kt \quad (1)$$

where C_0 and C are the contaminant concentrations at the beginning and during light illumination, respectively, k is the reaction rate constant, and t is time (Raghavan et al. 2015). The photocatalytic efficiency can be represented by reaction rate constant, k, which is also the slope in Fig. 5b. It can be seen that when the number of PSS/TiO_2 bilayers is higher, k is also higher, and the value of k gets saturated when the number of bilayers is 4. This means a number of PSS/TiO_2 bilayers greater than 4 will not significantly change the photodegradation efficiency. This is because the bottom photocatalyst was covered by the upper photocatalyst, and only the upper photocatalyst could receive light illumination and photodegrade MB. When the number of PSS/TiO_2 is 4, $k = 0.0173/\text{min}$.

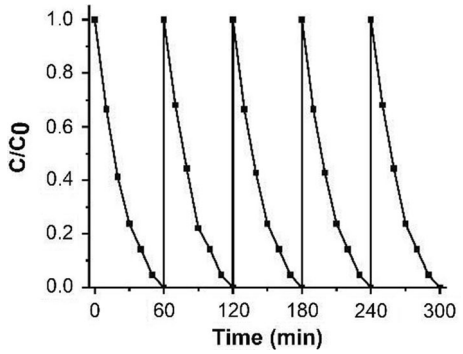

Fig. 7 Relative MB concentration versus irradiation time in cycling test

The same tests were done in different numbers of PSS/TiO_2 bilayers on a glass substrate and rGO/TiO_2 bilayers on a shrink polymer substrate. The results are shown in Fig. 6.

Figure 6 shows that the PSS/TiO_2 bilayers on a glass substrate always have the lowest photocatalytic efficiency, and the highest photocatalytic efficiency observed was $k = 0.0106/\text{min}$. The highest photocatalytic efficiency was obtained in shrink polymer with 6 rGO/TiO_2 bilayers. The highest reaction rate constant was $k = 0.0222/\text{min}$, 2.1 times higher than PSS/TiO_2 bilayers on glass substrate and 1.28 times higher than PSS/TiO_2 bilayers on a shrink polymer substrate.

The high photocatalytic efficiency for rGO/TiO_2 bilayers on a shrink polymer can be attributed primarily to two reasons: the high surface area induced by shrink and enhanced electron transfer due to graphene material. As the original size of shrink polymer is 6.25 times higher than the size after shrinking and covering the glass, the amount of immobilized photocatalyst is also higher than cover glass. The enhancement of photocatalytic efficiency by introducing graphene material has been verified by many publications. Even though the amount of TiO_2 in rGO/TiO_2 bilayers is less than PSS/TiO_2 bilayers, the enhanced electron transfer prevents photoexcited electron–hole recombination, and improves the photocatalytic efficiency even beyond PSS/TiO_2 bilayers.

The cycling tests were also performed to show the long-term stability of LBL self-assembled rGO/TiO_2 bilayers on shrink polymer. A sample with 4 rGO/TiO_2 bilayers on shrink polymer was used for this test. 10 mL MB solution with 10 μM concentration was fully degraded within 1 h. The process was repeated 5 times, and the result was shown in Fig. 7. It can be inferred from the figure that no decrease of photocatalytic efficiency was observed, which means that the bonding between photocatalyst and substrate is firm, and the result is repeatable.

4 Conclusions

This study shows that the photocatalyst can be firmly immobilized on glass substrates and shrink thermoplastic films using LBL self-assembly. The folds structure induced by shrinking helps increase photocatalytic efficiency by 63%, and the introduction of graphene material further enhances the photocatalytic efficiency to 2.1 times higher than pure TiO_2 immobilized on a glass substrate. Overall, more than 70% of 100 μM MB was removed in 1 h using rGO/TiO_2 bilayers immobilized on a shrink thermoplastic film, and the 10 μM MB can be fully removed within 1 h.

Acknowledgements Portions of this work were conducted in the Minnesota Nano Center, which is supported by the National Science Foundation through the National Nano Coordinated Infrastructure Network (NNCI) under Award Number ECCS-1542202. This work was partially sponsored by Environment and Natural Resources Trust Fund (ENRTF) funding in Minnesota State.

References

Al-Mathloom AR, Abed AA (2019) Titanium dioxide thin film prepared by sol-gel technique. J Educ Pure Sci Univ Thi-Qar 9(1):241–258

Alotaibi AM, Sathasivam S, Williamson BA, Kafizas A, Sotelo-Vazquez C, Taylor A, Scanlon DO, Parkin IP (2018) Chemical vapor deposition of photocatalytically active pure brookite TiO_2 thin films. Chem Mater 30(4):1353–1361

Cunha DL, Kuznetsov A, Achete CA, da Hora Machado AE, Marques M (2018) Immobilized TiO_2 on glass spheres applied to heterogeneous photocatalysis: photoactivity, leaching and regeneration process. PeerJ 6:e4464

De Lasa HI, Serrano B, Salaices M (2005) Photocatalytic reaction engineering. Springer, New York, p 193

De Villiers MM, Otto DP, Strydom SJ, Lvov YM (2011) Introduction to nanocoatings produced by layer-by-layer (LbL) self-assembly. Adv Drug Deliv Rev 63(9):701–715

Desa UN (2016) Transforming our world: the 2030 agenda for sustainable development

Fujishima A, Zhang X, Tryk DA (2008) TiO_2 photocatalysis and related surface phenomena. Surf Sci Rep 63(12):515–582

Guo J, Zhu S, Chen Z, Li Y, Yu Z, Liu Q, Li J, Feng C, Zhang D (2011) Sonochemical synthesis of TiO_2 nanoparticles on graphene for use as photocatalyst. Ultrason Sonochem 18(5):1082–1090

Klesko JP, Rahman R, Dangerfield A, Nanayakkara CE, L'Esperance T, Moser DF, Peña LF, Mattson EC, Dezelah CL, Kanjolia RK, Chabal YJ (2018) Selective atomic layer deposition mechanism for titanium dioxide films with (EtCp) Ti $(NMe_2)_3$: ozone versus water. Chem Mater 30(3):970–981

Li P, Zhang B, Cui T (2015) TiO_2 and shrink induced tunable nano self-assembled graphene composites for label free biosensors. Sens Actuators B Chem 216:337–342

Liu Y, Wang A, Claus R (1997) Molecular self-assembly of TiO_2/polymer nanocomposite films. J Phys Chem B 101(8):1385–1388

Manga KK, Zhou Y, Yan Y, Loh KP (2009) Multilayer hybrid films consisting of alternating graphene and titania nanosheets with ultrafast electron transfer and photoconversion properties. Adv Funct Mater 19(22):3638–3643

Padoin N, Andrade L, Ângelo J, Mendes A, Moreira RDFPM, Soares C (2016) Intensification of photocatalytic pollutant abatement in microchannel reactor using TiO_2 and TiO_2-graphene. AIChE J 62(8):2794–2802

Pera-Titus M, GarcÍa-Molina V, Baños MA, Giménez J, Esplugas S (2004) Degradation of chlorophenols by means of advanced oxidation processes: a general review. Appl Catal B Environ 47(4):219–256

Raghavan N, Thangavel S, Venugopal G (2015) Enhanced photocatalytic degradation of methylene blue by reduced graphene-oxide/titanium dioxide/zinc oxide ternary nanocomposites. Mater Sci Semiconduct Process 30:321–329

Safardoust-Hojaghan H, Salavati-Niasari M (2017) Degradation of methylene blue as a pollutant with N-doped graphene quantum dot/titanium dioxide nanocomposite. J Clean Prod 148:31–36

Wang Y, Ding X, Chen X, Chen Z, Zheng K, Chen L, Ding J, Tian X, Zhang X (2017) Layer-by-layer self-assembly photocatalytic nanocoating on cotton fabrics as easily recycled photocatalyst for degrading gas and liquid pollutants. Cellulose 24(10):4569–4580

Williams G, Seger B, Kamat PV (2008) TiO_2-graphene nanocomposites. UV-assisted photocatalytic reduction of graphene oxide. ACS Nano 2(7): 1487-1491

Yao HB, Wu LH, Cui CH, Fang HY, Yu SH (2010) Direct fabrication of photoconductive patterns on LBL assembled graphene oxide/PDDA/titania hybrid films by photothermal and photocatalytic reduction. J Mater Chem 20(25):5190–5195

Zhang H, Lv X, Li Y, Wang Y, Li J (2010) P25-graphene composite as a high performance photocatalyst. ACS Nano 4(1):380–386

Simulation and Experiments on a Valveless Micropump With Fluidic Diodes Based on Topology Optimization

Peng Zhou, Tianyi Zhang, Terrence W. Simon, and Tianhong Cui, *Senior Member, IEEE*

***Abstract*— Micropumps are microelectromechanical system (MEMS) devices that pump small quantities of liquids. They are used in many applications such as electronics cooling and drug delivery. Valveless fluid diode micropumps with no moving parts have recently attracted great interest in the MEMS community. In this paper, topology optimization is used to design two-dimensional, fixed-geometry, fluidic diodes of high diodicity, which is the ratio of pressure drops of forward to reverse flows. One of the fluidic diodes, of the Tesla type, shows a diodicity of over five. Another is of the nozzle-diffuser type. Both are experimentally and computationally demonstrated herein. Then the numerical simulation was applied to simplify the structures, and the two-dimensional geometry was converted into three-dimensional model for micropumps. Three-dimensional and unsteady numerical analyses of micropump fluid flow with optimized diodes were conducted for pumps of each of the two diode designs. The micropump with the Tesla-type fluidic diode reached a measured flow rate of 34 ml/h, consistent with the computed results and 2.2 times that of the nozzle-diffuser type micropump. The performance results show a high dependence on internal channel geometry. The two types show highest flow rates with an internal channel thickness of 200 μm. Demonstrated good repeatability and precise flow control show positive prospects for application. [2021-0144]**

***Index Terms*— Fluidic diode, topology optimization, valveless pump.**

I. Introduction

MICROPUMPS are microelectromechanical systems (MEMS) devices that pump small quantities (nanoliters or microliters) of fluid. They have been widely used in thermal control of electronics, measurement of volumes in the micro-scale, mixing of microfluidic streams, and medical applications [1]. For example, the piezoelectric actuation based valveless micropump has proved to be useful for drug delivery [2], and its application as an actuator for dynamic cultures on 'organs on a chip' has gained recent attention [3]. Passive fluid diodes with no mechanical moving parts are used in valveless micropumps. They have attracted great interest due to their simple structures, compact sizes, lack of electromagnetic interferences, and easy integration [4]. The working mechanism of the valveless micropump is based on the difference of flow resistance between forward flow and back flow through internal channels [5].

Two commonly used valveless micropumps are based on either nozzle-diffuser channels or Tesla-type diodes. The nozzle-diffuser valveless micropump uses V-shaped channels that behave like nozzles when the flow is in one direction and like diffusers when the flow is in the opposite direction [4], [6], [7]. Chandrasekaran and Packirisamy studied the flow behavior of a nozzle-diffuser type valveless micropump with geometrical tuning using finite element modeling [8]. They proposed a method to design the best diffuser geometries using different diffuser angles. Then Yang and his group considered increasing the micropump flow rate by adding two-fin, or obstacle, structures into the nozzle-diffuser design [9]. However, the increased flow resistance offset the potential improvement. The Tesla-type valveless micropump gained interest after 1999 because of its high diodicity. Researchers [10] considered different structures of the Tesla valve flow-directing element. The diodes are complex channels (to be introduced below) that offer different flow losses for the two flow directions. Derakhshan *et al.* simulated flow behavior of the Tesla-type valveless micropump and optimized the dimensions of the diode to achieve higher diodicity and flow rate [11]. Kolahdouz suggested that the two-stage Tesla valve is the optimized design for a piezoelectric-driven micropump [12]. Most of the published work is focused on dimension or shape optimization of existing flow-directing elements [13]. Since the fundamental structures are not changed, performance improvement was limited.

Topology optimization is a systematic approach to optimize the layout of valve internal elements using a computational procedure for a given set of boundary conditions and constraints [14]. It has been successfully used to solve fluid-based problems, especially in the design of fluidic diodes with high diodicity [15]. Lin *et al.* used this method to optimize the Tesla-type valve and obtained fluidic diodes with diodicities of up to 8.87 [16]. Sato and his group proposed a bi-objective topology optimization method and designed a fluidic diode with lower pressure drop for the forward flow and higher pressure drop for the backward flow [17]. The published fluidic diodes were mainly used as fluidic resistance valves [18], and their application to valveless pumps was barely discussed.

Manuscript received July 9, 2021; revised October 25, 2021; accepted November 20, 2021. Date of publication December 28, 2021; date of current version April 4, 2022. This work was supported in part by the Minnesota Environment and Natural Resources Trust Fund as recommended by the Legislative-Citizen Commission on Minnesota Resources (LCCMR) and in part by the Minnesota Nano Center by the National Science Foundation through the National Nano Coordinated Infrastructure Network (NNCI) under Award ECCS-1542202. An earlier version of this paper was presented at the IEEE 34th International Conference on Micro Electro Mechanical Systems, in January 2021 [DOI: 10.1109/MEMS51782.2021.9375273]. Subject Editor H. Jiang. *(Corresponding author: Tianhong Cui.)*

The authors are with the Department of Mechanical Engineering, University of Minnesota, Minneapolis, MN 55455 USA (e-mail: zhou1161@umn.edu; zhan6202@umn.edu; simon002@umn.edu; cuixx006@umn.edu).

This article has supplementary material provided by the authors and color versions of one or more figures available at https://doi.org/10.1109/JMEMS.2021.3133469.

Digital Object Identifier 10.1109/JMEMS.2021.3133469

Moreover, the scales of these published fluidic diodes were large relative to MEMS devices, further preventing application to MEMS-based micropumps [18].

This work seeks to investigate a microscale fluidic diode of high diodicity that can be used in valveless micropumps to achieve higher mass flow rate by using topology optimization and computational fluid dynamic (CFD) methods. MEMS technology is used to fabricate the fluidic diode-based valveless micropumps.

II. Experiments and Analysis

A. Topology Optimization

The two-dimensional fluidic diode was first obtained using topology optimization based on the Density Model with Darcy interpolation. In short, the Navier-Stokes equations for forward and backward flows were solved. The ratio of pressure drop between the inlet and outlet for backward flow and forward flow was calculated as diodicity. To achieve high diodicity, the ratio of energy dissipation between backward and forward flow was set as the objective function for topological optimization [19]. A relatively low Reynold number of 100 was used for the calculation. The scale of a fluidic diode is primarily defined by the width of the inlet chamber. The different widths of the outlet and sizes of the computational domains were used to obtain fluidic diodes of different geometries. The diodicity of each fluidic diode was calculated to evaluate its performance.

The designed fluidic diodes with the highest diodicity were selected to employ in a valveless pump. The structure of the selected fluidic diode of the Tesla-type design was first simplified to remove extremely small features that cause excessive aspect ratios of the features that can challenge the fabrication process. The removed small structures are unnecessary and have little effect on performance. The performance characteristics of three-dimensional fluidic diodes of both types and of various thicknesses were also evaluated to optimize the thickness of valveless micropump.

Finally, CFD simulations of valveless micropumps with the selected fluidic diodes were applied. The nozzle-diffuser type valveless micropump of the same actuator size was simulated for comparison.

Commercial software COMSOL Multiphysics was used to solve the topology optimization for 2D structures, and CFD simulation was conducted for 2D and 3D structures by ANSYS Fluent.

B. Fabrication and Evaluation

MEMS technology was used to fabricate the valveless micropump with the topologically optimized Tesla-type fluidic diodes and with the conventional nozzle-diffuser diode to fabricate valveless micropumps for comparison. In order to capitalize upon repeated use of molds and low-cost processing technology, micropumps with a sandwich structure of two polymer films and an intermediate structural layer were designed and fabricated [20].

The fabrication process is shown in Fig. 1a. Lithography with negative photoresist SU8-100 was first performed on a silicon wafer. The thickness of the photoresist ranged from 150 μm to 250 μm, depending on the rotational speed of

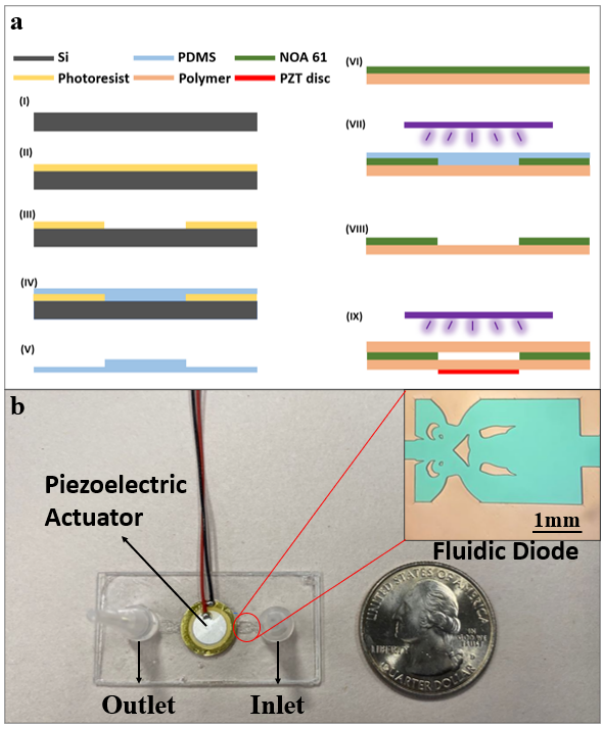

Fig. 1. (a) Schematic diagram of the fabrication process; (b) picture of the valveless micropump with the designed Tesla-type fluidic diode and a microscope image of the detailed structure.

the spin coating process. Polydimethylsiloxane (PDMS) was then poured on a silicon-based mold and cured to obtain a soft mold with mating structures. Then UV-curing glue, NOA61, was applied on the PDMS mold and covered with a UV-transparent polymer film. The NOA61 was partially cured under UV illumination, followed by replacement of the PDMS mold with another polymer sheet. More UV illumination was then applied to fully cure the NOA61. Finally, a piezoelectric (PZT) disc was attached to a polymer film to serve as the actuator. Fig. 1b shows details of the critical structures of the fabricated fluidic diode based valveless micropump based on the Tesla diode.

Characterization mainly includes measuring the amplitude of the PZT actuator (Fig. 1b), the flow rate of the micropump, and the pressure difference under operation. A function generator and a linear piezoelectric amplifier were used as the excitation source of the PZT actuator. A voltage of up to 100 V was applied to the PZT disc. The amplitude of the PZT actuator movement was measured by a laser vibrometer. The inlet and outlet of the micropump were connected to tubes of known diameters. The mass flow rate was calculated by placing the inlet and outlet tubes horizontally at the same level and measuring the displacement of the liquid meniscus in the tube within a specific period. In the pressure difference test, the inlet and outlet tubes were placed vertically and the pressure difference was determined by measuring the liquid level difference.

III. Results and Discussion

Figures 2a and 2b show the computational domain before and after topology optimization. The size of the inlet and outlet, and the length and width of the rectangular computational domain were optimized for high diodicity.

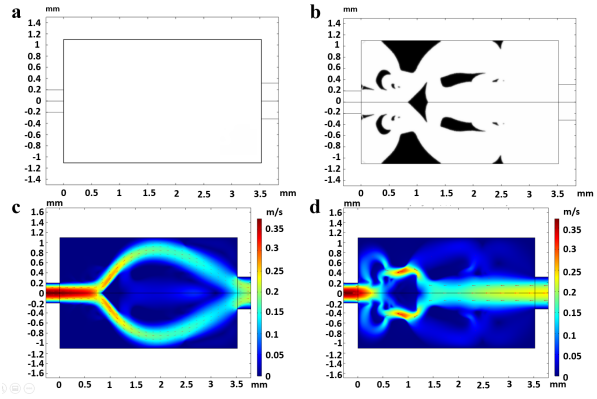

Fig. 2. (a) Computational domain for topology optimization; (b) fluidic diode geometry after topology optimization; (c) velocity contours of forward flow through the fluidic diode; (d) velocity contours of backward flow through the fluidic diode.

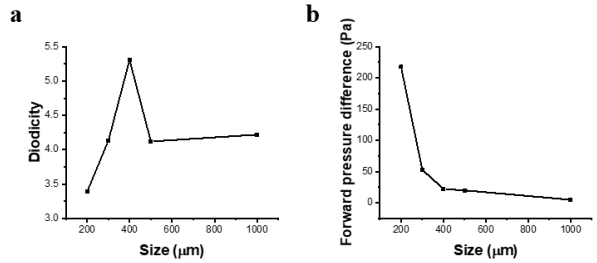

Fig. 3. (a) Highest diodicity of Tesla-type fluidic diode of different sizes; (b) pressure difference of fluidic diode with highest diodicity of different sizes.

The resulting geometry with the highest diodicity is shown in Fig. 2b. This figure also shows the geometry of a typical Tesla-type diode. The through-flow velocity contours for forward and backward flows through the fluidic diode are shown in Figures 2c and 2d. The backward flow is divided into several tributaries which then interact with one another at their confluence, leading to more resistance in the backward flow than in the forward flow. The diodicity of the fluidic diode is calculated by the ratio of backward flow pressure drop to forward flow pressure drop. It is 5.31 in this work.

Fig. 3a shows the optimized diodicity of fluidic diodes of different inlet sizes. The highest diodicity appears with an inlet size of 400 μm. The diodicity of smaller fluidic diodes is limited by the feature sizes, which has a great effect on the device fabrication while the diodicity of larger fluidic diodes is limited by the degrees of freedom during the optimization calculation. Too many elements leads to excessive degrees of freedoms and failure of convergence. Fig. 3b shows the corresponding forward pressure difference of fluidic diodes of different channel inlet sizes. The smaller pressure difference means smaller flow resistance and lower power needed to drive the pump. As the size of fluidic diode increases, the pressure difference first decreases, then tends to level off. The fluidic diode with an inlet chamber size of 400 μm was selected for further simulation.

Topology optimization was performed on a two-dimensional (infinite depth) geometry, which allows viscous forces on the side walls to be neglected. However, the height of the actual microchannel is limited and is always comparable to the other two dimensions. Thus, it is important to consider the effect

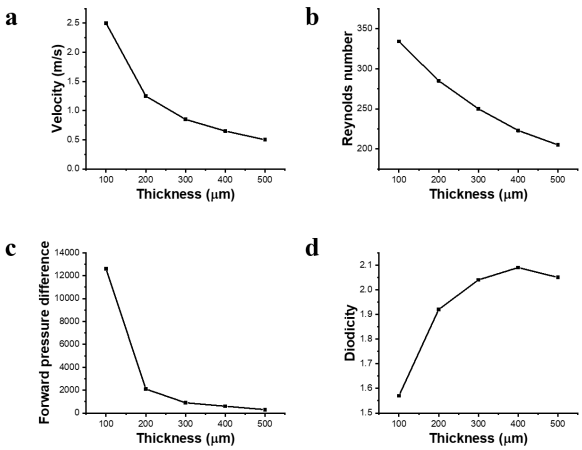

Fig. 4. The effects of thickness on (a) velocity, (b) Reynolds number, (c) pressure difference, and (d) diodicity of the Tesla-type designed fluidic diode.

of thickness on the performance of the designed fluidic diode. To address this, a three-dimensional analysis was performed by CFD simulation. When converting the simulation of the fluidic diode from two-dimensions to three, the mass flow rate of 0.1 g/s was used for calculation and depths ranging from 100 μm to 500 μm were studied. Fig. 4 shows the velocity, Reynolds number, pressure difference, and diodicity of fluidic diodes of various thicknesses. The results show that larger thickness leads to smaller velocities and Reynolds numbers due to the fixed mass flow rate. The diodicity is reduced because of the smaller associated inertial forces. On the other hand, the effects of viscous forces are more significant when the thickness is less, leading to higher pressure differences but lower diodicities. The simulation was conducted for a valveless micropump using a 200 μm thick microchannel.

Before the simulation of the Tesla-type valveless micropump with the chosen fluidic diode, the structure of the fluidic diode was simplified for lower complexity and easier fabrication. Fig. 5a shows the structure and diodicity of the original design. As shown in Fig. 5b, all structures smaller than 20 μm were removed to avoid fabrication of high-aspect-ratio features, and the diodicity was reduced from 1.92 to 1.90. Small structures with little effect on diodicity were also removed, resulting in a diodicity of 1.89 (Fig. 5c). Any further simplification (as in Fig. 5d) leads to significant reduction of diodicity. Therefore, the structure in Fig. 5c was employed in the valveless micropump with Tesla-type fluid diodes.

Simulation of valveless micropumps was conducted by CFD. The geometry used for simulation is shown in Fig. 6a. The two fluidic diodes are connected by an actuator chamber attached to a PZT actuator and the other ends are connected to the inlet and outlet chambers. The thickness of fluidic diode and actuator chamber was set as 200 μm. The fluid parameters were set according to water at room temperature. The transient laminar flow model with the SIMPLE pressure treatment algorithm and second-order upwind interpolation was used for the simulation.

The diameter of the chamber having the attached PZT actuator was 10 mm. The amplitude of oscillation of the center of the actuator was set as 5 μm, matching optimum experimental results. The changes in displacement over time follows a

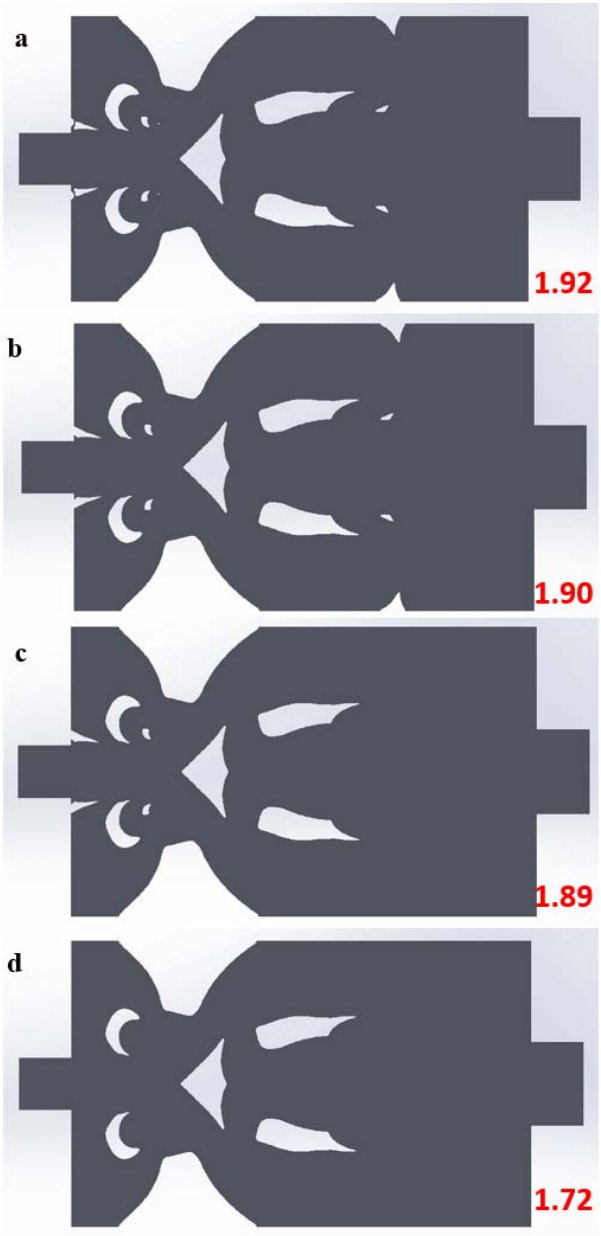

Fig. 5. Structure and diodicity of (a) original designed Tesla-type fluidic diode; (b) fluidic diode with small structure removed; (c) fluidic diode with unnecessary structure removed; (d) fluidic diode with critical structure removed.

sinusoidal wave function. The deflection profile of the PZT actuator can be divided into two sections: the inner section, with piezoelectric ceramics, and the outer section, with brass (see Fig. 6a). When a sinusoidal excitation voltage is applied to the PZT disc, the piezoelectric ceramic section vibrates. The brass section also vibrates. The deflection of these two sections can be described by the following equations [21]:

$$d_1(r) = d_{max}[1 + (b^2r^2 - a^2r^2)/(2a^2b^2ln(a/b))]sin(2\pi ft), \quad (0 \le r \le a) \tag{1}$$

$$d_2(r) = d_{max}[(b^2 + 2b^2ln(r/b) - r^2)/(2b^2ln(a/b))]sin(2\pi ft), \quad (a \le r \le b) \tag{2}$$

where the d_1 and d_2 are the deflections of the inner and outer sections, respectively; d_{max} is the amplitude of the membrane center, which is set as 5 μm; a is the radius of the inner section, which is 3.75 mm; b is the diameter of outer section, which is 5 mm; f is the excitation frequency, which is 200 Hz.

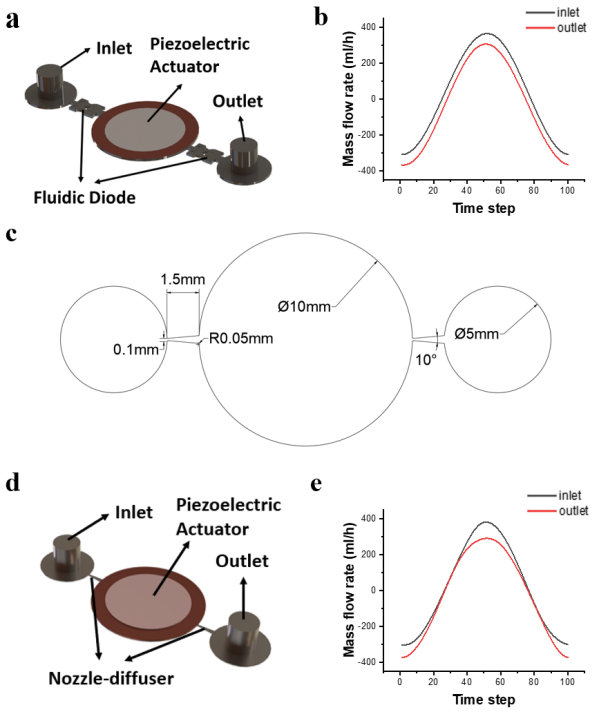

Fig. 6. (a) a schematic of the Tesla-type valveless micropump; (b) a plot of the mass flow rate for the Tesla-type valveless micropump; (c) critical parameters for the nozzle-diffuser type valveless micropump; (d) a schematic of the nozzle-diffuser type valveless micropump; (e) a plot of the mass flow rate for the nozzle-diffuser valveless micropump.

Dynamic meshing with a User Defined Function (UDF) was applied to describe the movement of the piezoelectric actuator. The pressures of the inlet and outlet surfaces were set to zero and the mass flow rates at the inlet and outlet surfaces were monitored. A mesh sensitivity study was performed first to make sure that the results were independent of mesh quantity, and a mesh with 4.2 million nodes was chosen for the simulations. Each cycle was divided into 100 time-steps, leading to a time step size of 50 μs. The details for the mesh and time-step independence studies can be found in the supplemental materials.

The mass flow rate through the micropump with the fluidic diodes in the inlet and outlet passages was calculated, as shown in Fig. 6b. The positive mass flow means water flow into the micropump, while the negative mass flow means the water flow out of the micropump. It can be found from the figure that when the water is pumping out, the outlet has a higher mass flow rate, and the inlet has a higher mass flow rate when the water is pumping in. The mass flow rate difference between inlet and outlet, integrated over time, leads to the net mass flow rate of the micropump. The net mass flow rate of 31.3 ml/h was calculated as the cycle average.

The same simulation was performed on the nozzle-diffuser type valveless micropump. The critical parameters of the nozzle-diffuser are shown in Fig. 6c, obtained from work done by He *et al.* [22]. The other parameters are the same as those of the Tesla-type fluidic diode-based valveless micropump. Fig. 6d shows the structure of the micropumps used for the simulation.

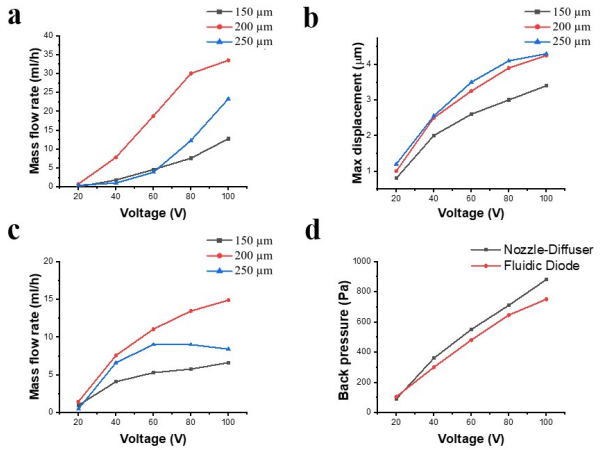

Fig. 7. (a) Mass flow rate of the fluidic diode-based valveless micropump in various thicknesses; (b) the maximum displacement of the center of the PZT actuator for the fluidic diode-based valveless micropump in various thickness; (c) the mass flow rate of the nozzle-diffuser type valveless micropump in various thicknesses; (d) back pressure of the two different types of valveless micropumps 200 μm thick.

The mass flow rate of the nozzle-diffuser type valveless micropump was calculated based on the inlet and outlet mass flow rate difference, as shown in Fig. 6e. The simulated mass flow rate was 20.6 ml/h, 34.2% lower than with the Tesla-type fluidic diode-based valveless micropump. Comparing Figures 6b and 6e shows that both micropumps have high diodicity at high flow velocity while the Tesla-type fluidic diode-based valveless micropump has better performance at lower flow rates. This is consistent with the high diodicity of the designed Tesla-type fluidic diode under low Reynolds number conditions.

To verify the simulation results and optimize the working conditions of the valveless micropumps, both the Tesla-type fluidic diode and the nozzle-diffuser type valveless micropumps of various thicknesses were fabricated using the process described in Fig. 1a.

Fig. 7a shows the measured mass flow rates of the Tesla-type diode micropump operating under different excitation voltages. As discussed previously, there is no inlet-to-outlet pressure difference for this flow measurement. As shown, the mass flow rate increases as the excitation voltage increases. The reason can be found in Fig. 7b, showing the maximum displacement of the center of the PZT actuator under different excitation voltages. Higher excitation voltage leads to larger displacements of the PZT actuator, resulting in increased mass flow rates. This micropump of 200 μm thickness has a higher mass flow rate than the ones of 150 μm and 250 μm thicknesses. This suggests that the inertial and viscous forces reach a balance under an optimum thickness of 200 μm, producing higher diodicity and mass flow rate. The different flow rates when the inlet-to-outlet pressure difference is zero, different maximum displacement of the PZT actuator, and different pressure differences when flow rate is zero are shown in Figures 7a, 7b, and 7c, respectively, each for three different thicknesses. The highest mass flow rate achieved is 33.5 ml/h. The difference between simulation results and experimental data is about 7%, lending credibility to the results from CFD simulation.

Three nozzle-diffuser type valveless micropumps with different thicknesses were fabricated for comparison. The mass flow rates of the nozzle-diffuser type valveless micropumps in different thickness were also measured, as shown in Fig. 7c. As with the Tesla-type fluidic diode-based micropumps, the mass flow rate increases with excitation voltage and the micropump of 200 μm thickness has a higher mass flow rate, compared to the pumps of other thicknesses. The highest mass flow rate achieved by the nozzle-diffuser type valveless micropumps is 14.9 ml/h, 44% of the valveless micropump with the Tesla-type designed fluidic diodes. Comparing the experimental results with the simulation results shown in Fig 6e, the computational calculation is 38% overestimated. The gap between measurements and computation is mainly due to the lower displacement of the actuator in real testing. The vibration amplitude of the actuator for the nozzle-diffuser and designed fluidic diode valveless pump was set the same in CFD simulation. However, the nozzle-diffuser has a higher forward pressure difference than the designed fluidic diode, therefore the PZT actuator cannot achieve the same amplitude as diode-based micropumps do when the same voltage is applied.

The pressure differences of the two different types of valveless micropumps, both 200 μm thick, were measured and compared. Recall that this measurement was taken without flow. As shown in Fig. 7d, the nozzle-diffuser type micropump has a higher pressure difference than the Tesla-type fluidic diode-based micropump. This is as expected because the designed Tesla-type fluidic diode has a small pressure difference, as shown in Fig. 4c. Although the designed Tesla-type fluidic diode has high diodicity, its pressure differences are relatively low. However, the mismatch of pressure difference between the two valveless micropumps is only around 10%. Relative to the 2.2 times enhancement of the mass flow rate for the Tesla-type diode micropump, this small difference of pressure drop is justified.

IV. Conclusion

This work provides an efficient design process for developing a high-performance fluidic diode-based valveless micropump. A two-dimensional fluidic diode was first obtained by topology optimization. The diodicity reached 5.31 with a Reynolds number of 100. Then the thickness and layout of the Tesla-type designed fluidic diode were optimized and deployed in the valveless micropump. The performance of the proposed valveless micropump was evaluated by both CFD simulation and experiments. The result shows that the high diodicity of the Tesla-type designed fluidic diode leads to better performance at low Reynolds numbers among the two valveless micropumps. It was proven that the valveless micropump of 200 μm thickness with the designed Tesla-type fluidic diode can achieve 2.2 times the mass flow rate of the traditional nozzle-diffuser type valveless micropump. A large number of applications will benefit from the high flow rate of the designed valveless micropump. For example, more efficient mixing caused by stronger convection can be expected when the valveless micropump is used for mixing of microfluidic streams. Also, higher throughput for drug delivery and stronger actuation for 'organs on a chip' can be expected.

Acknowledgment

The numerical part of this work was carried out using computing resources at the University of Minnesota Supercomputing Institute.

REFERENCES

[1] S. Hanasoge, P. J. Hesketh, and A. Alexeev, "Microfluidic pumping using artificial magnetic cilia," *Microsyst. Nanoeng.*, vol. 4, no. 1, pp. 1–9, Dec. 2018.

[2] R. R. Gidde, P. M. Pawar, and V. P. Dhamgaye, "Fully coupled modeling and design of a piezoelectric actuation based valveless micropump for drug delivery application," *Microsyst. Technol.*, vol. 26, no. 2, pp. 633–645, Feb. 2020.

[3] S. Mi, H. Pu, S. Xia, and W. Sun, "A minimized valveless electromagnetic micropump for microfluidic actuation on organ chips," *Sens. Actuators A, Phys.*, vol. 301, Jan. 2020, Art. no. 111704.

[4] E. Stemme and G. Stemme, "A valveless diffuser/nozzle-based fluid pump," *Sens. Actuators A, Phys.*, vol. 39, no. 2, pp. 159–167, Nov. 1993.

[5] K. Mohammadzadeh, E. M. Kolahdouz, E. Shirani, and M. B. Shafii, "Numerical study on the performance of Tesla type microvalve in a valveless micropump in the range of low frequencies," *J. Micro-Bio Robot.*, vol. 8, nos. 3–4, pp. 145–159, Dec. 2013.

[6] X. N. Jiang, Z. Y. Zhou, X. Y. Huang, Y. Li, Y. Yang, and C. Y. Liu, "Micronozzle/diffuser flow and its application in micro valveless pumps," *Sens. Actuators A, Phys.*, vol. 70, nos. 1–2, pp. 81–87, Oct. 1998.

[7] H. A. Dereshgi and M. Z. Yildiz, "Investigation of electro-mechanical factors effecting piezoelectric actuator for valveless micropump characteristics," *J. Eng. Sci. Technol.*, vol. 13, no. 9, pp. 2843–2856, 2018.

[8] A. Chandrasekaran and M. Packirisamy, "Geometrical tuning of microdiffuser/nozzle for valveless micropumps," *J. Micromech. Microeng.*, vol. 21, no. 4, Apr. 2011, Art. no. 045035.

[9] K.-S. Yang, T.-F. Chao, I. Y. Chen, C.-C. Wang, and J.-C. Shyu, "A comparative study of nozzle/diffuser micropumps with novel valves," *Molecules*, vol. 17, no. 2, pp. 2178–2187, Feb. 2012.

[10] F. K. Forster, R. L. Bardell, A. P. Blanchard, M. A. Afromowitz, and N. R. Sharma, "Micropumps with fixed valves," U.S. Patent 5 876 187, Mar. 2, 1999.

[11] S. Derakhshan *et al.*, "Performance improvement and two-phase flow study of a piezoelectric micropump with Tesla nozzle-diffuser microvalves," *J. Appl. Fluid Mech.*, vol. 12, no. 2, pp. 341–350, Mar. 2019.

[12] E. M. Kolahdouz, "Design and fabrication of a piezoelectrically actuated micropump using modified Tesla type microvalves," M.S. thesis, Dept. Mech. Eng., Isfahan Univ. Technol., Isfahan, Iran, 2010.

[13] Q. Yan, Y. Yin, W. Sun, and J. Fu, "Advances in valveless piezoelectric pumps," *Appl. Sci.*, vol. 11, no. 15, p. 7061, Jul. 2021.

[14] O. Sigmund and K. Maute, "Topology optimization approaches," *Struct. Multidisciplinary Optim.*, vol. 48, no. 6, pp. 1031–1055, Dec. 2013.

[15] J. Alexandersen and C. S. Andreasen, "A review of topology optimisation for fluid-based problems," *Fluids*, vol. 5, no. 1, p. 29, Mar. 2020.

[16] S. Lin, L. Zhao, J. K. Guest, T. P. Weihs, and Z. Liu, "Topology optimization of fixed-geometry fluid diodes," *J. Mech. Design*, vol. 137, no. 8, Aug. 2015, Art. no. 081402.

[17] Y. Sato, K. Yaji, K. Izui, T. Yamada, and S. Nishiwaki, "Topology optimization of a no-moving-part valve incorporating Pareto frontier exploration," *Struct. Multidisciplinary Optim.*, vol. 56, no. 4, pp. 839–851, Oct. 2017.

[18] Y. Deng, Z. Liu, P. Zhang, Y. Wu, and J. G. Korvink, "Optimization of no-moving part fluidic resistance microvalves with low Reynolds number," presented at the IEEE 23rd Int. Conf. Micro Electro Mech. Syst. (MEMS), Hong Kong, Jan. 2010.

[19] M. P. Bendsoe and O. Sigmund, *Topology Optimization: Theory, Methods, and Applications*. Berlin, Germany: Springer, 2013.

[20] T. H. Yoon, S. H. Park, K. I. Min, X. Zhang, S. J. Haswell, and D.-P. Kim, "Novel inorganic polymer derived microreactors for organic microchemistry applications," *Lab a Chip*, vol. 8, no. 9, pp. 1454–1459, 2008.

[21] S. Yang, S. Q. Yuan, S. C. Cai, D. D. Wei, and X. H. He, "A valveless piezoelectric micropump based on Coanda effect," *Trans. Chin. Soc. Agricult. Eng.*, vol. 45, pp. 343–348, Mar. 2014.

[22] X. He, J. Zhu, X. Zhang, L. Xu, and S. Yang, "The analysis of internal transient flow and the performance of valveless piezoelectric micropumps with planar diffuser/nozzles elements," *Microsyst. Technol.*, vol. 23, no. 1, pp. 23–37, Jan. 2017.

[23] P. Zhou, T. Zhang, T. Simon, and T. Cui, "A fluidic diode and its application to a valveless micropump," presented at the IEEE 34th Int. Conf. Micro Electro Mech. Syst. (MEMS), Jan. 2021.

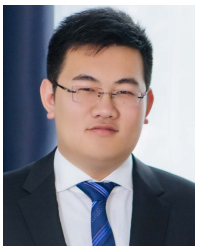

Peng Zhou was born in Ningguo, Anhui, China, in 1993. He received the B.S. degree from the Department of Mechanical Engineering, Beijing Institute of Technology, China, in 2015, and the M.S. degree in mechanical engineering from Purdue University Northwest, USA. He is currently pursuing the Ph.D. degree with the Department of Mechanical Engineering, University of Minnesota, guided by Prof. T. Cui.

His research interests include the photocatalytic water purification and MEMS-based microsensors for both environmental and biomedical applications.

Tianyi Zhang was born in Qinhuangdao, Hebei, China, in 1990. He received the B.S. and Ph.D. degrees from the Department of Mechanical Engineering, Xi'an Jiaotong University, Xi'an, Shanxi, China, in 2013 and 2019, respectively.

He spent one year as a Visiting Scholar at the University of Minnesota, where he is currently a Post-Doctoral Associate with the Department of Mechanical Engineering. His research interests include vibration mode coupling in micromechanical resonators and oscillators and mass transport in electrochemical sensing applications.

Terrence W. Simon received the B.S. degree in mechanical engineering from Washington State University, Pullman, WA, USA, in 1968, the M.S. degree in mechanical engineering from the University of California at Berkeley, Berkeley, CA, USA, in 1971, and the Ph.D. degree in mechanical engineering from Stanford University, Stanford, CA, USA, in 1980.

He is the Ernst G. Eckert Professor with the Department of Mechanical Engineering. His major research interests include experiments, computation, and visualization of heat, mass, and momentum transfer in laminar, turbulent, transitional, and unsteady flows, including flows through porous media and processes with phase change. Applications range from flow and heat transfer in plasma cutting tools and plasma flow actuators, electronics and optics, Stirling and gas turbine engines, and MW-level grid energy storage systems.

Dr. Simon is an Active Member of the American Society of Mechanical Engineers (including a past five-year term as the Senior Technical Editor of the *Journal of Heat Transfer*), the International Centre for Heat and Mass Transfer (in which he is now the President and has served on the Executive Committee), and the American Society of Thermal and Fluids Engineers (for which he co-chaired the International Workshop on Heat Transfer in 2017).

Tianhong Cui (Senior Member, IEEE) received the B.S. degree in mechanical engineering from the Nanjing University of Aeronautics and Astronautics in 1991 and the Ph.D. degree in mechanical engineering from the Chinese Academy of Sciences in 1995.

He is currently a Distinguished McKnight University Professor at the University of Minnesota. From 1995 to 2003, he held research or faculty positions at Tsinghua University, the University of Minnesota, the National Laboratory of Metrology, Japan, and Louisiana Tech University, before he joined the Faculty at the University of Minnesota. His research interests include MEMS and NEMS. He has more than 340 archived publications in scientific journals and prestigious conferences. He is an Adjunct Professor at Mayo Clinic, a Distinguished Visiting Fellow at the University of Cambridge, and a Distinguished Visiting Professor at the University of Paris-Est, France.

Dr. Cui is a fellow of the American Society of Mechanical Engineering (ASME). He is the Founding Executive Editor-in-Chief of *Microsystems & Nanoengineering* (Nature). He is also serving as the Founding Editor-in-Chief of the first AAAS/Science Partner Journal titled *Research*.

Sensors & Actuators: B. Chemical 354 (2022) 131218

Contents lists available at ScienceDirect

Sensors and Actuators: B. Chemical

journal homepage: www.elsevier.com/locate/snb

Vibrating an air bubble to enhance mass transfer for an ultra-sensitive electrochemical sensor

Tianyi Zhang, Peng Zhou, Terrence Simon, Tianhong Cui *

Department of Mechanical Engineering, University of Minnesota, 111 Church Street SE, Minneapolis, MN 55455, USA

ARTICLE INFO

Keywords:
Vibrating air bubble
Streaming flow
Mass transfer
Electrochemical sensor
Anodic stripping voltammetry

ABSTRACT

Rapid mass transfer of analytes is essential for effective electrochemical sensing. Here, we present a vibrating air bubble as a stirrer and evaluate the optimal working frequency. A vibration system that contains a flexible piezoelectric plate coupled with a trapped bubble integrated with a gold working electrode is employed. The vibrational properties and mass transfer of the coupled system are experimentally tested with optical and electrochemical methods, respectively. Streaming flows generated by the vibrating bubble are characterized by visualization to explain the enhancement of mass transport to the working electrode. Compared with a static case, measurements with a vibrating bubble demonstrate a twelve-times enhancement in mass transfer coefficient. Enhanced sensing performance is experimentally quantified with the bubble stirrer and its integrated electrochemical metal ion sensor. This integrated system can be used for various types of electrochemical sensing applications that are limited by slow molecular diffusion.

1. Introduction

Electrochemical methods have drawn considerable attention in chemical and biological detection due to their significant advantages, such as low cost and high sensitivity [1,2]. Normally, for sensing, analytes in the solution, such as metal ions, nucleic acids, and proteins, must accumulate on the surface of the working electrode [3–5]. This requires mass transfer, which includes diffusion, convection, and migration [6]. In static solutions, this process is usually limited by a slow molecular diffusion rate that may take hours for sensing [7], causing a major obstacle to the sensing performance. To overcome this problem, methods involving convective mass transport can be employed. By generating fluid motion near the working electrode, the diffusion layer thickness can be reduced and the molecular transmission rate through the diffusion layer to the reaction interface can be aided by convection [8].

Among various methods of generating liquid flow, streaming flows induced by a vibrating air bubble in the liquid are of increasing interest in recent years [9,10]. The streaming flow of interest in the present paper is due to nonlinear second-order effects in the fluid mechanics that are induced by unsteady surface deformations of a vibrating air bubble [11]. In contrast to a mechanical stirrer, this strategy does not need a movable mechanical component near the sensor, which makes the vibrating bubble a low-cost, low-power, easy-to-integrate method for production of circulating flow. Bubble induced streaming flow has already been utilized in multiple microfluidic applications, such as micropumps [12], chemical switches [13], micromixers [14], microswimmers [15], and acoustic manipulation of organic cells or particles [16]. Detailed classification and introduction of the applications employing streaming flows are summarized in several review papers [17–19].

In the above-mentioned works, vibrating air bubbles are trapped in a rigid structure. Acoustic waves are generated by a piezoelectric transducer attached to the substrate. The waves propagate within the structure to vibrate the bubbles. The optimized working frequencies for bubbles to produce streaming flows, normally considered to be resonance frequencies of the bubble, are usually determined by experiments conducted while documenting with particle image velocimetry (PIV) measurements [20,21]. Such PIV measurement is complicated and time-consuming. Moreover, it has a poor frequency resolution and cannot be used to track the resonance frequency of the bubble in real-time. However, the resonance frequency of a bubble can be directly measured with a laser Doppler vibrometer using a laser spot focused directly on the surface of the bubble [22–24]. The accuracies of both amplitude and frequency using this method can be extremely high. But such measurements can be influenced by the liquid itself, and the

* Corresponding author.
E-mail addresses: zhan6202@umn.edu (T. Zhang), zhou1161@umn.edu (P. Zhou), simon002@umn.edu (T. Simon), cuixx006@umn.edu (T. Cui).

https://doi.org/10.1016/j.snb.2021.131218
Received 21 September 2021; Received in revised form 29 November 2021; Accepted 5 December 2021
Available online 9 December 2021

container sidewalls, which limit their applicability. Also used are flexible piezoelectric energy harvesters that detect the vibrational amplitude of a bubble [25] by converting the vibration of the bubble to a voltage signal through a piezo-electric pickup.

Here we propose a stirring strategy for electrochemical measurement, where a piezoelectric-actuated vibrational air bubble stirrer is integrated with a working electrode. A novel method, aiming to detect the resonance frequency and optimal working frequencies of the vibrating air bubble, is demonstrated based on mechanical vibration coupling between the bubble and a flexible plate. In this work, the vibrating system includes a flexible piezoelectric plate coupled to a trapped air bubble, in which the vibrational energy is transferred from the plate to the bubble. The vibrational properties of the coupled system are experimentally investigated with a laser Doppler vibrometer, and the resonance frequency and optimal working frequencies of the bubble are directly related to the frequency response of the piezoelectric plate. Streaming flows induced by the vibrating bubble are characterized by dye tracing under different working frequencies. These flows can be utilized to accelerate mass transport of analytes from the bulk solution toward the sensing electrode surface. With an integrated working electrode and the electrochemical method, we measured the mass transfer coefficient under the influence of the streaming flows. Finally, the performance of the air bubble stirrer with the integrated electrode is evaluated as an electrochemical metal ion sensor.

2. Material and methods

2.1. Reagents

Reagents are potassium ferricyanide (III), potassium chloride, bismuth standard solutions (1000 mg/L in 5% HNO_3), and methylene blue, all purchased from Sigma-Aldrich (St. Louis, MO, United States), and Hydrochloric acid (1.0 N) and sulfuric acid (98%), purchased from Fisher Scientific (Hampton, NH, United States). All solutions are prepared with deionized water from AmeriWater silex deionization system (Dayton, OH, United States).

2.2. Fabrication of bubble actuator and working electrode

A piezoelectric vibrating bubble actuator attached with a working electrode for electrochemical measurements was designed and fabricated in this study. The exploded 3D view and the cross-section of the integrated device are shown in Fig. 1(a) and (b), respectively. The fabrication process consists of four components: A piezoelectric plate (15 mm and 10 mm in diameter for the metal plate and piezoelectric ceramic) are attached to a pre-cut polymethyl methacrylate (PMMA) frame. A circular hole (10 mm in diameter) is cut by a laser cutter. A polyimide (PI) film (25 μm thick) is bonded to the bottom layer of the piezoelectric plate (the metal side), followed by attachment of a polytetrafluoroethylene (PTFE) ring onto the PI surface, located at the center of the plate. The PTFE ring acts as the bubble trapper having inner and outer diameters of 1.7 mm and 2.3 mm. A PMMA thin film (300 μm thick) is cut with a laser to form the contour of the electrode substrate, then is cleaned with ethanol and deionized water. The central hole (4 mm in diameter) is used to accommodate the PTFE ring. The PMMA film is covered by a polyester (PE) shadow mask also fabricated with the laser cutter. Subsequently, a gold layer (100 nm thick) is sputtered onto the PMMA film to form the working electrode. Finally, the working electrode is attached to the PMMA frame. The gap between the PI film and the working electrode substrate is 500 μm. The working electrode and the piezo plate are connected to wires with silver adhesive. A photo of the fabricated device is shown in Fig. S1 of the supplemental material.

2.3. Characterization of vibration and streaming flow

The experimental setup is shown in Fig. 1(b). A laser Doppler

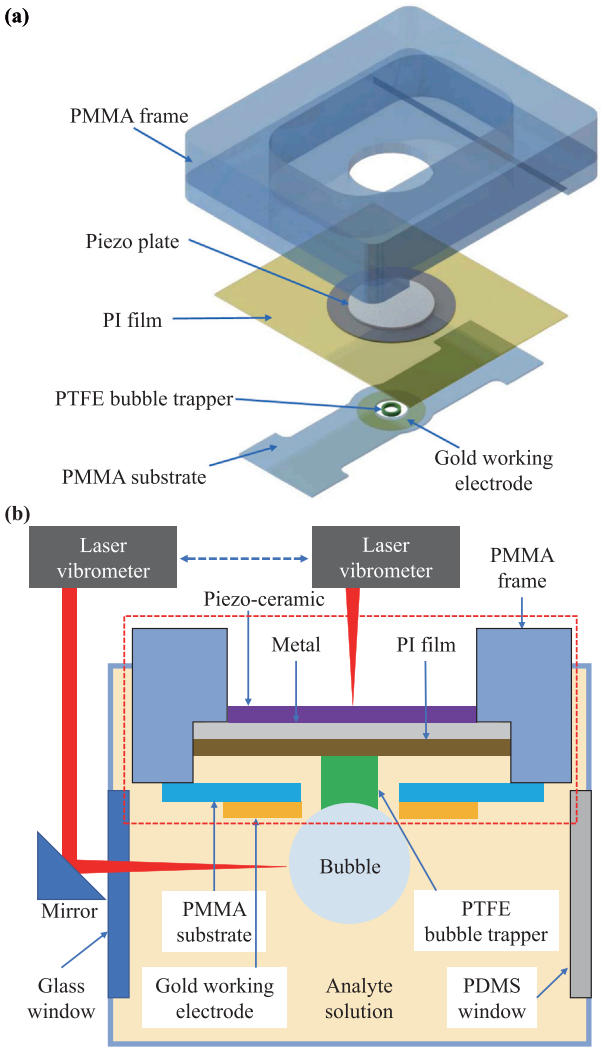

Fig. 1. (a) Exploded 3D view of the vibrating bubble actuator with an attached gold working electrode. (b) Cross-sectional schematic of the device (shown in the red dashed box) and a schematic of the experimental setup.

vibrometer (PSV-400 Polytec Inc., Irvine, CA, United States) is used to characterize the vibrational properties of the piezoelectric plate and the trapped air bubble. The driving alternating voltage is applied by a built-in function generator and is amplified by a linear piezoelectric amplifier (VF-500, Dynamic Structures and Materials, Franklin, TN, United States) before driving the piezoelectric ceramic. The integrated device is placed horizontally in a self-made PMMA cuboid container filled with deionized water. There is a glass window on three sidewalls of the container and a polydimethylsiloxane (PDMS) window on the last sidewall. The glass window is for light transmission, while the PDMS window is used to pass the needle through to introduce the bubble gas. A photo of the device with the container is shown in Fig. S1 in the supplemental material. To measure the vibrational properties of the piezo plate, a vertical laser beam from the laser vibrometer is used to scan the upper surface of the piezoelectric ceramic. A 45-degree tilted mirror is employed to steer the laser beam to be horizontal to detect vibration of the air bubble. In the horizontal beam case, the laser beam is carefully focused on the tangent point between the bubble surface and the vertical plane. The movement of the piezo plate in the out-of-plane direction and the amplitude of the bubble are detected successively by the vibrometer.

The air bubble is injected with a needle through the PDMS window and placed on the PTFE bubble trapper. The volume of the bubble is controlled by a microliter pipette connected to the needle. Dye

(10 mmol/L methylene blue) is injected near the bubble by a syringe needle. Optical images of the bubble and dye are captured with a high-speed camera (GS3-U3-23S6M-C, FLIR Systems, Wilsonville, OR, United States) by viewing through the glass window, together with an LED light source located on the opposite side of the container.

2.4. Mass transfer tests and metal ion detection

An electrochemical workstation (PGSTAT302N Metrohm, Riverview, FL, United States) is employed for characterization of the mass transfer coefficient and for metal ion detection, using chronoamperometry and anodic stripping voltammetry (ASV) methods, respectively. A platinum wire (1 mm in diameter) and an Ag/AgCl (in 3.0 mol/L KCl solution) electrode are used as the counter and reference electrodes, respectively. Before the electrochemical measurement is conducted, the gold working electrode is cleaned with the cyclic voltammetry method (from −0.4 V to 1.5 V vs. Ag/AgCl at a scan rate of 0.1 V/s) for 40 scans in a 1 mol/L H_2SO_4 solution.

The chronoamperometry measurement is conducted in a 2 mmol/L $K_3Fe(CN)_6$/0.5 mol/L KCl solution. A conditioning potential of 0.7 V is applied on the gold working electrode for 90 s prior to each measurement. The working potential for mass transfer characterization is − 0.4 V, and the measurement lasts for 90 s, while bubble vibration is maintained. The following four steps are carried out for each of the ASV tests in a 20 ppb Bi^{3+}/0.1 mol/L HCl solution: conditioning the working electrode, background scan, metal deposition and the analytical scan. The conditioning potential is 0.7 V, and the conditioning time is 30 s longer than the deposition time. The square wave voltammetry (SWV) method is used in the two steps of scanning. The SWV parameters are the following: scan window is − 0.3–0.7 V; square wave amplitude and frequency are 25 mV and 25 Hz, respectively; and step potential is 5 mV. In the metal deposition step, the deposition potential is − 0.3 V, and the deposition time is from 30 to 150 s. The bubble vibration is maintained during only the deposition step.

3. Results and discussion

3.1. Characterization of vibrating bubble system and streaming flow

The vibrational properties of the piezo plate and the air bubble are characterized by measuring their frequency responses with the laser Doppler vibrometer. The gold working electrode is removed in this experiment and the following dye tracing experiment to ensure good vision of the bubbles and flow. The piezoelectric ceramic is driven by a frequency chirp signal (from 0.1 to 6 kHz) with an ultra-small voltage amplitude (0.01 V) to avoid generation of complex surface modes of the bubble [26]. Then the detected signal from the surface vibration of the piezo plate and air bubble is subjected to a fast Fourier transform to obtain the response in frequency space at a specific vibrometer scan location. We also measured the mode shape of the piezo plate by scanning the whole surface of the ceramic part of the plate with the vibrometer. Frequency response curves measured at the center point of the piezo plate, where the bubble trapper is located, are shown in Fig. 2(a). When there is no bubble, a single resonance peak is observed (black curve), corresponding to the (0, 1) mode of the circular piezo plate vibrating in a liquid environment. The mode number of (0, 1) is determined by checking the measured mode shape, as shown in Fig. 2(c). The color scale used in the mode shape figures of Fig. 2(c) represents vibrating velocity distributions. The red parts are anti-nodes where the velocity has its maximum value. After an air bubble is placed onto the bubble trapper, the frequency response measurement is taken again. Now, the frequency response curves indicate that the original single resonance peak of the plate is split into two peaks by a deep valley in the middle, making the frequency response curve of the plate appear as a capital letter M (seen for the other four curves excluding the black curve in Fig. 2(a)). It is found by checking the mode shapes obtained at each of

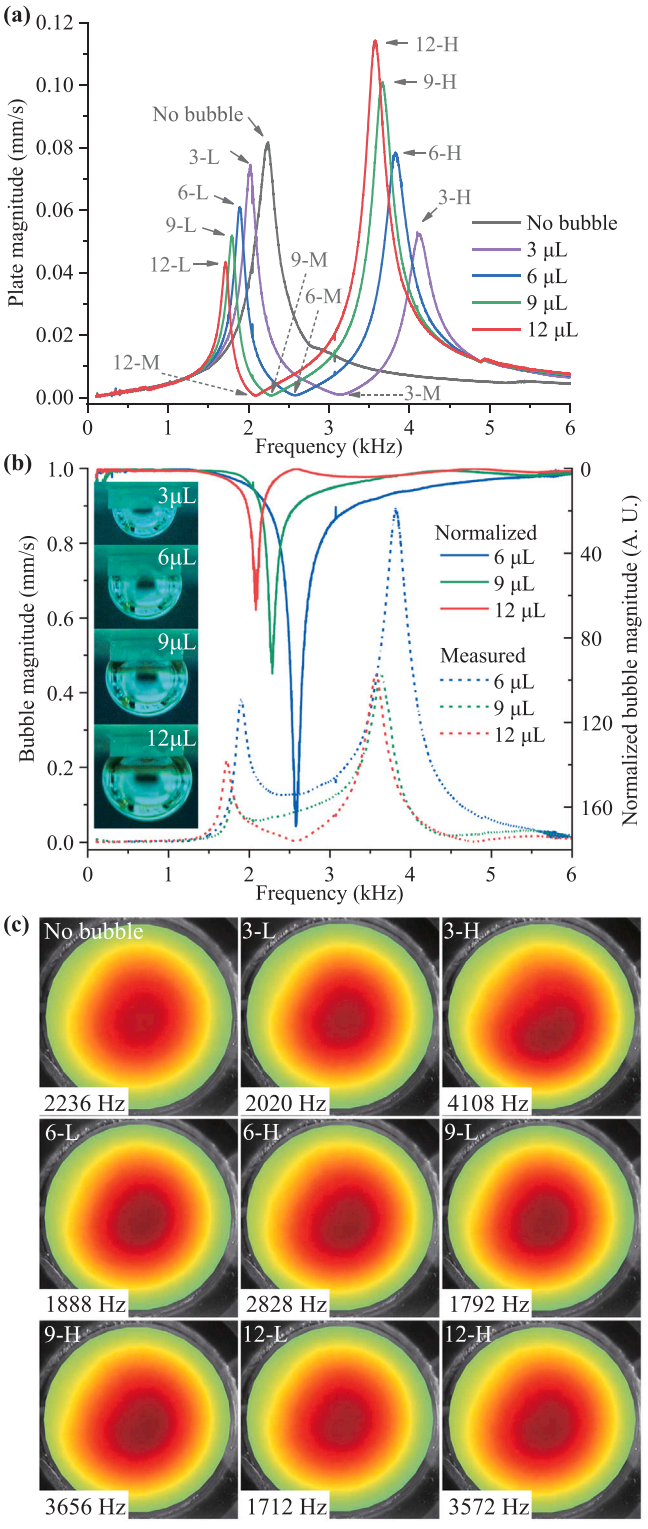

Fig. 2. (a) Frequency response measured at the center point of the piezoelectric plate's upper surface. (b) Frequency response measured at the surface of the air bubble (dashed line) and normalized frequency response of the vibrating bubble (solid line). Inserts are the optical images of different volumes of bubbles. (c) 2D mode shape obtained by the laser vibrometer. Each figure corresponds to a marked peak in (a). The driving amplitude is 0.01 V in all the measurements. Letters L, M and H correspond to the lower peak, middle valley and higher peak observed in (a), respectively.

the peak frequencies in Fig. 2(c) that both peaks of a single curve belong to the same vibration mode (the (0, 1) mode). To further reveal the mechanism of this phenomenon, the frequency response of the air bubble is directly measured with a 45-degree tilted mirror (see Fig. 1 (b)). The absence of a corresponding dashed line in Fig. 2(b) indicates that a bubble of 3 μL volume cannot be detected since its small size failed to generate a tangent point for laser focus. The normalized frequency response of the air bubble is calculated by dividing the frequency response of the bubble by the frequency response of the plate, as shown on the solid lines in Fig. 2(b). Three clear resonance peaks can be observed. They correspond to the intrinsic frequency responses of different sizes of bubbles. A comparison of Fig. 2(a) and (b) shows that the resonance frequency of the bubble is the same as the frequency of the deep valley (the lowest point of the valley, labeled by the dashed arrows in Fig. 2(a)). Considering the vibrating plate and the bubble as two coupled vibration modes, such phenomenon can be explained as an internal resonance between plate and bubble [27]. The deep valley is induced by energy transfer from the piezo plate to the air bubble. The transfer efficiency can reach its maximum value at the resonance frequency of the bubble, leading to a minimum value infrequency response of the plate. By coupling an air bubble to a flexible piezo plate through a bubble trapper, the resonance frequency of the bubble can be obtained by checking the frequency response of the piezoelectric plate. This is much more convenient and simpler than the more difficult and challenging method of using laser Doppler vibrometry or particle image velocimetry to measure bubble vibration. There are other low-cost methods for frequency response measurement of a piezoelectric transducer, such as impedance measurement [28].

Next, when we use the vibrating bubble to generate streaming flows, large vibrational amplitudes in the surface mode of a bubble are required for effective streaming [29]. Three working conditions are considered, according to the dynamic characteristics of the coupled system: vibrating at the frequency of the lower peak, the bottom of the middle valley, and the higher frequency peak (represented by L, M, and H). Optical images of a 9 μL bubble are captured with a high-speed camera using an exposure time of 0.005 ms. The driving voltages for the three conditions are 0.5, 0.6, and 0.4 V, respectively, to maintain a similar vibrating velocity for the L and H conditions, and a relatively higher velocity for the M condition. The images are shown in Fig. 3(a), where the velocities are the values measured at the center point of the piezo plate. All three working conditions can generate surface modes, indicating the possibility of producing streaming flows. Streaming flows are qualitatively characterized by injecting a small amount of methylene blue dye (10 mmol/L in deionized water) near the 9 μL bubble. The driving voltage is kept constant during the image capture experiment. The dye distribution images are shown in Fig. 3(b). For the lower and higher peak conditions, when the plate center has a vibrating velocity of 150 mm/s or more, significant streaming of the flow is observed, but the two streams are in opposite directions. When vibrating at the lower peak frequency, liquid under the bubble is moved upward, then is ejected laterally to form vortices. When the driving frequency is at the higher peak value, the liquid around the bubble is collected, then jetted vertically downward, to generate vortices. If the piezo plate is driven at the bottom of the middle valley frequency (resonance frequency of the bubble), a streaming flow can also be detected, but it is extremely weak. It is most likely caused by the small amplitude of the bubble compared with the amplitudes under the lower peak and higher peak conditions. The red arrows in Fig. 3(b) indicate the direction of the streaming flows, where the solid and dashed lines refer to non-vortical flow and vortical flow, respectively. The dye experiment discussed above is conducted also, by using a vibrating plate and without a bubble. No streaming flow is detected when vibration is initiated. A video of the no-bubble condition, as well as videos of each figure in Fig. 3 are included in the supplemental material. It seems that both lower and higher peak working conditions can transport fresh solution from distant fluid to the vicinity of the air bubble, which is expected to enhance mass transfer. Especially

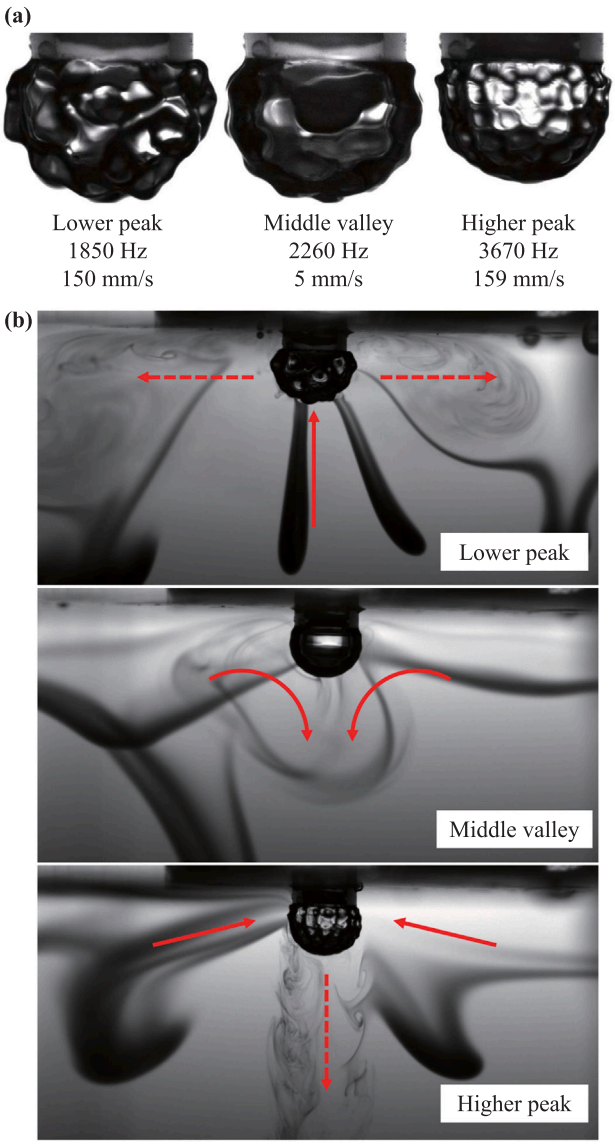

Fig. 3. (a) Optical images of a vibrating bubble at different driving frequencies identified in Fig. 2(a). (b) Streaming flow marked with methylene blue dye near the vibrating bubble. The solid and dashed arrows represent non-vortical flow and flow with vortices, respectively. In all the experiments, the volume of the bubble is 9 μL. Vibrating velocities shown in (a) are measured at the center point of the piezoelectric plate's upper surface. Full videos of the streaming are available in the supplemental material.

for the lower peak condition, the streaming flow generates vortices near the plate surface where the gold working electrode is located. In the next section, mass transfer capabilities with different bubble vibrating conditions are tested using electrochemical methods.

3.2. *Electrochemical experiment with a vibrating bubble*

Mass transfer coefficients under the influence of streaming flows induced by the vibrating bubble are measured with the chronoamperometry method using 2 mmol/L $K_4[Fe(CN)_6]$ as the oxidizing agent. On the working electrode, $[Fe(CN)_6]^{4-}$ is reduced into $[Fe(CN)_6]^{3-}$ with a working potential of − 0.4 V vs. Ag/AgCl reference electrode. The current, induced by the reduction reaction, is used to characterize the mass transfer coefficient since the process is a mass transfer dominant reaction. A 90-second test is applied in each measurement during which the current almost reaches steady state. The

current (proportional to the reaction rate) plotted as a function of time for different bubble working conditions is shown in Fig. 4(a). The lower peak, middle valley, and higher peak for the 9 μL bubble, as well as the condition without a bubble, are measured for various vibrating velocities of the plate. All the working conditions show an increasing trend in current with vibrating velocity, even without a bubble, since vibration of the circular membrane itself generates flow motion and enhances mass transfer [30]. Note that for different bubble vibrating conditions, the steady state current shows a different fluctuation range. The current for each condition of the largest velocities range is within the 0.03 mA range on the Y-axis, shown separately in Fig. S2 of the supplement. For no bubble and middle valley conditions, the current fluctuation is almost as small as that of the static case, since no streaming flow and only a tiny non-vortical flow are observed in these two cases. An increased current fluctuation and large current values are found under the higher-peak conditions. An even higher current value, but a huge current fluctuation, is obtained when the lower peak is used. These two results correspond to the two streaming flow directions in Fig. 3(b). There exists a strong non-vortical flow near the substrate when using the higher peak condition, and a complex pattern of vortices covers the surface of the substrate, when under the lower-peak condition. We calculated the average current in the last five seconds of the test at which a steady state current is reached and plotted it as a function of vibrating velocity of the piezo plate, as shown in Fig. 4(b). The vibrating velocity is selected as a reference quantity since the mass transfer is directly related to the velocity [31]. Although the middle valley condition (vibrating at the resonance frequency of the air bubble) can produce over five times the mass transfer enhancement at a very small plate actuation velocity, such a working frequency is not a good choice if a large mass transfer coefficient is expected. The dynamic characteristics of the coupled system limit the actual amplitude of the bubble to a small value. Operation at the lower and higher peaks are two operational options. The mass transfer coefficients are enlarged 12 and 10 times, respectively, according to the currents measured. The lower peak condition, with a higher mass transfer rate and fluctuation, can be used in electrochemical sensing methods that require only an accumulation of analytes, such as anodic stripping voltammetry (ASV) [32] or adsorptive stripping voltammetry (AdSV) [33]. The higher peak condition, with lower mass transfer rate (still has at least one order of magnitude enhancement) but a smaller fluctuation, can be employed with sensing techniques that need real-time measurement, such as chronoamperometry [34]. In addition, we measured the reduction current with different volumes of bubbles (3, 6, and 12 μL) using the lower peak as the working frequency. Directly measured results are shown in Fig. S3 of the supplement. The steady-state current as a function of plate vibrating velocity is shown in Fig. 4(c). The larger bubbles give higher mass transfer coefficients with plate vibration velocities of the same level. However, a larger bubble more easily becomes unstable under a strong driving force. Occasionally the bubble, or a part of a bubble will escape from the trapper. This led to fewer successful experiments and fewer results for the 12 μL bubble test. Besides, as a coupled system, resonance characteristics of the bubble actuator, which is a piezoelectric plate in this work, must also be considered if optimized performance is expected. This is because the frequencies and amplitudes when operating at the lower and higher peak conditions are determined by both the piezoelectric plate and the bubble dynamics.

Finally, to evaluate the potential application of vibrating bubbles in electrochemical sensors, anodic stripping voltammetry (ASV) is used to detect bismuth ions in a solution (20 ppb Bi^{3+} in 0.1 mol/L HCl). Stripping voltammetric analysis is a well-established electrochemical technique frequently used in metal ion concentration measurement. The significant advantages of such a method include easy operation, low cost, and high sensitivity [35]. In ASV analysis, the peak current height or peak area of the anodic wave is used to quantify the amount of analyte in the solution, which depends on the accumulation of reduced metal [36]. A 9 μL bubble is attached and the piezo plate is driven at the lower

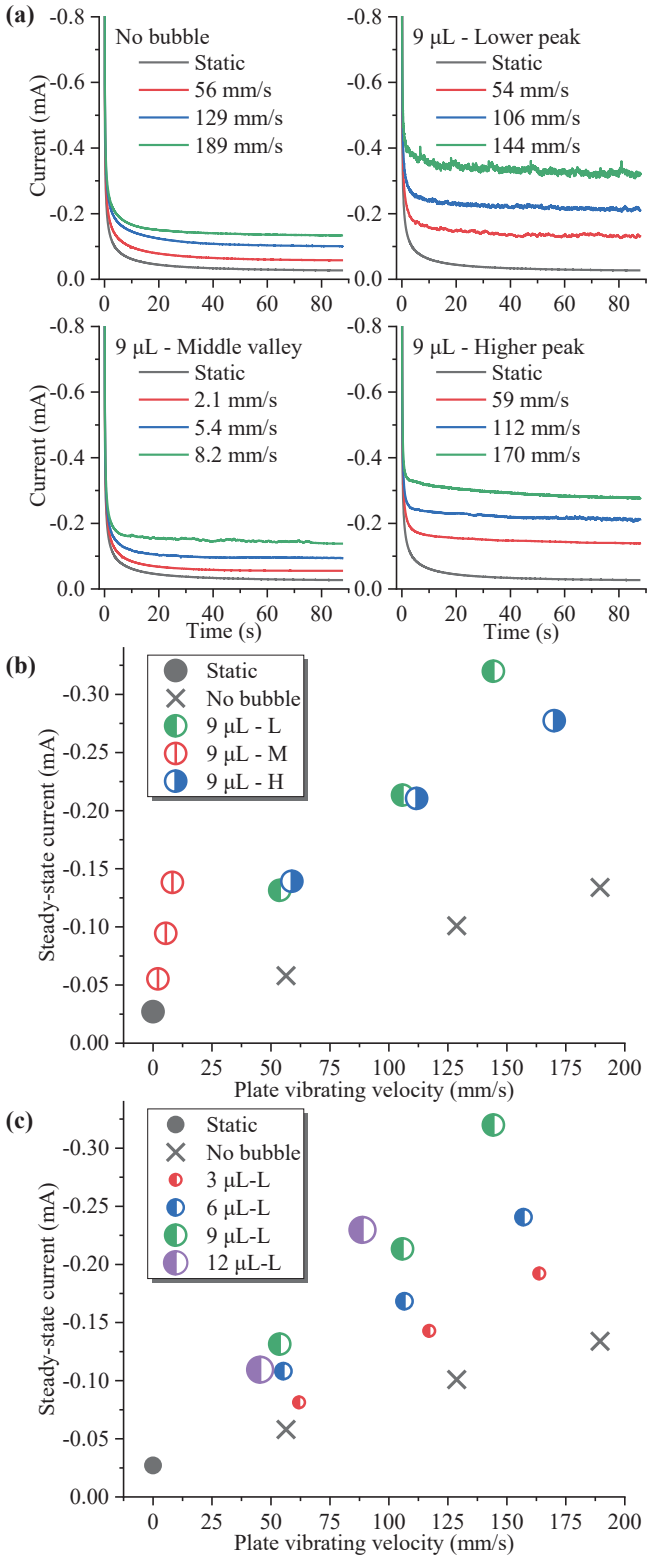

Fig. 4. (a) Chronoamperometry measurement results of the working electrode without bubble (upper left) and with bubble (a 9 μL bubble vibrating at different driving frequencies). (b) and (c) are measured steady-state current as a function of vibrating velocity of the piezoelectric plate. Results for a 9 μL bubble at different driving frequencies are shown in (b), and for different volumes of bubbles at the lower peak frequency are shown in (c). Above experiment is operated in 2 mmol/L $K_4[Fe(CN)_6]$/0.5 mol/L KCl with an electrochemical working potential of − 0.4 V vs. Ag/AgCl.

peak frequency with a velocity of about 100 mm/s. The vibration is activated only during the metal deposition process. The stripping curves are obtained by subtracting the background scan from the analytical scan. The results with and without bubble vibration are shown in Fig. 5 (a). As the deposition time increases from 30 s to 150 s, the height of the stripping peak gradually increases because more bismuth is oxidized during the stripping process. Meanwhile, the stripping peaks under vibrating conditions are much larger than the peaks in the static condition. This is due to the different mass transfer coefficients in the metal deposition process. The stripping peak height is calculated and plotted as a function of deposition time in Fig. 5(b). The bars indicating variability are obtained using four independent measurements. The bars for the vibrating conditions are larger than those for the static case, mostly attributed to vibrating amplitude drift within the series of repeated measurements. The frequency response of the coupled system shows some shift, especially after a long period of vibration. In addition, the stripping peak under the vibrating condition shows a slightly nonlinear increase with deposition time. Such a phenomenon may be explained by the increase in working electrode roughness (increase in surface area) resulting from solid metal deposition [37]. Considering a relatively linear range within deposition time from 30 to 120 s, linear fit curves are plotted in Fig. 5(b). R-Squared correlation values for static and vibrating conditions are 0.995 and 0.992, respectively. The peak current and deposition time can be considered as an approximately linear relationship in this range, in which the slope represents the sensor output increment (peak current) induced by a unit of deposition time. The slope for the static and vibrating conditions are 0.018 and 0.135 μA per second, respectively, demonstrating that the vibrating bubble stirrer accelerates the detection speed of the sensor by over 7 times. These data show that the mass transfer coefficient can be greatly enhanced by streaming flows produced by a vibrating bubble, as the detection speed of the sensor is boosted.

4. Conclusion

In this paper, a vibrating air bubble as a stirrer for an electrochemical sensor is presented. The vibrating system contains a flexible piezoelectric plate coupled to a trapped air bubble, both residing in the liquid environment. A gold working electrode for electrochemical sensing is integrated within the system. The resonance frequency and optimal streaming flow generating frequencies of the air bubble are determined based on the mechanical coupling between the piezo plate and the bubble. Streaming flows generated by the vibrating air bubble are employed to enhance mass transfer efficiency of the integrated working electrode.

From the optical measurement of the vibrational properties of the coupled system, it is found that energy is transferred from the piezo plate to the air bubble, leading to an M-shaped frequency response of the plate. The M-shaped velocity vs. frequency curve contains two peaks and one valley, corresponding to two potential working frequencies for streaming generation, and the resonance frequency of an air bubble. According to the dye tracing experiment, the streaming flows at the two optimal working frequencies (lower peak and higher peak frequencies) are in opposite directions. They can be utilized to study enhancement of mass transfer coefficients on the working electrode. Electrochemical tests indicate that the mass transfer rate increases as the vibration intensity of the piezo plate increases, improving by an order of magnitude compared to the static condition. The results obtained by anodic stripping voltammetry to detect bismuth ions also indicate that, with the help of a vibrating bubble, the sensing performance is significantly improved. We believe that such a design of a piezoelectric-actuated air bubble stirrer with an integrated working electrode can be very promising in electrochemical detection when higher mass transfer rates are required.

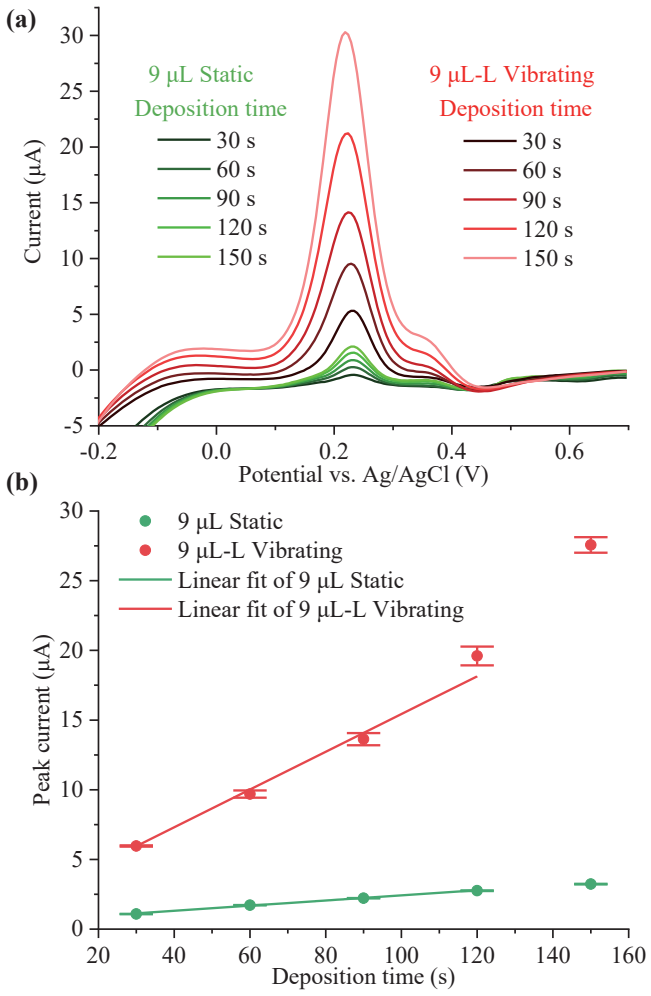

Fig. 5. (a) Anodic stripping voltammetry measurement results for the working electrode in the detection of Bi^{3+} with (red) and without (green) bubble vibration. The 9 μL bubble is driven at the lower peak frequency. (b) Measured stripping peaks as a function of deposition time under static and vibrating conditions (the range for linear fit is from 30 to 120 s). Error bars are calculated with four independent measurement results. The analyte solution contains 20 ppb Bi^{3+} and 0.1 mol/L HCl. The deposition potential is − 0.3 V vs. Ag/AgCl. The letter L represents the lower resonance peak of the piezo plate.

CRediT authorship contribution statement

Tianyi Zhang: Conceptualization, Methodology, Validation, Writing – original draft. **Peng Zhou**: Methodology, Validation. **Terrence Simon**: Methodology, Writing – review & editing. **Tianhong Cui**: Resources, Writing – review & editing, Supervision, Project administration.

Declaration of Competing Interest

The authors declare that they have no known competing financial interests or personal relationships that could have appeared to influence the work reported in this paper.

Acknowledgements

Portions of this work were conducted in the Minnesota Nano Center, which is supported by the National Science Foundation through the National Nano Coordinated Infrastructure Network (NNCI) under Award Number ECCS-2025124. This work was partially sponsored by Environment and Natural Resources Trust Fund (ENRTF) funding

through Legislative-Citizen Commission on Minnesota Resources (LCCMR) in Minnesota State.

Appendix A. Supporting information

Supplementary data associated with this article can be found in the online version at doi:10.1016/j.snb.2021.131218.

References

[1] J. Holmes, P. Pathirathna, P. Hashemi, Novel frontiers in voltammetric trace metal analysis: towards real time, on-site, in situ measurements, Trac Trends Anal. Chem. 111 (2019) 206–219, https://doi.org/10.1016/j.trac.2018.11.003.

[2] M.K. Masud, M. Umer, M.S.A. Hossain, Y. Yamauchi, N. Nam-Trung, M.J. A. Shiddiky, Nanoarchitecture frameworks for electrochemical miRNA detection, Trends Biochem. Sci. 44 (2019) 433–452, https://doi.org/10.1016/j.tibs.2018.11.012.

[3] A. Nsabimana, S.A. Kitte, T.H. Fereja, M.I. Halawa, W. Zhang, G. Xu, Recent developments in stripping analysis of trace metals, Curr. Opin. Electrochem. 17 (2019) 65–71, https://doi.org/10.1016/j.coelec.2019.04.012.

[4] E.E. Ferapontova, DNA electrochemistry and electrochemical sensors for nucleic acids, in: P.W. Bohn, J.E. Pemberton (Eds.), Annual Review of Analytical Chemistry, vol. 112018, pp. 197–218.

[5] E.V. Suprun, V.V. Shumyantseva, A.I. Archakov, Protein electrochemistry: application in medicine. A review, Electrochim. Acta 140 (2014) 72–82, https://doi.org/10.1016/j.electacta.2014.03.089.

[6] A.J. Bard, L.R.J.S.T. Faulkner, Electrochemical Methods Fundamentals and Applications, 20 (1983) 91–92.

[7] T. Kangkamano, A. Numnuam, W. Limbut, P. Kanatharana, T. Vilaivan, P. Thavarungkul, Pyrrolidinyl PNA polypyrrole/silver nanofoam electrode as a novel label free electrochemical miRNA-21 biosensor, Biosens. Bioelectron. 102 (2018) 217–225, https://doi.org/10.1016/j.bios.2017.11.024.

[8] C.S. Chapman, C.M.G. van den Berg, Anodic stripping voltammetry using a vibrating electrode, Electroanalysis 19 (2007) 1347–1355, https://doi.org/10.1002/elan.200703873.

[9] J. Jalal, T.S.H. Leong, Microstreaming and its role in applications: a mini-review, Fluids 3 (2018) 93, https://doi.org/10.3390/fluids3040093.

[10] Y. Gao, M. Wu, Y. Lin, J. Xu, Trapping and control of bubbles in various microfluidic applications, Lab a Chip 20 (2020) 4512–4527, https://doi.org/10.1039/d0lc00906g.

[11] S. Cleve, Microstreaming induced in the vicinity of an acoustically excited, nonspherically oscillating microbubble: Université de Lyon, 2019.

[12] Y. Gao, M. Wu, Y. Lin, W. Zhao, J. Xu, Acoustic bubble-based bidirectional micropump, Microfluid. Nanofluidics 24 (2020) 29, https://doi.org/10.1007/s10404-020-02334-6.

[13] D. Ahmed, C.Y. Chan, S.C. Lin, H.S. Muddana, N. Nama, S.J. Benkovic, T.J. Huang, Tunable, pulsatile chemical gradient generation via acoustically driven oscillating bubbles, Lab a Chip 13 (2013) 328–331, https://doi.org/10.1039/c2lc40923b.

[14] R.H. Liu, R. Lenigk, R.L. Druyor-Sanchez, J.N. Yang, P. Grodzinski, Hybridization enhancement using cavitation microstreaming, Anal. Chem. 75 (2003) 1911–1917, https://doi.org/10.1021/ac026267t.

[15] F.-W. Liu, Y. Zhan, S.K. Cho, Propulsion reversal in oscillating-bubble powered micro swimmer, J. Micromech. Microeng. 31 (2021), 084001, https://doi.org/10.1088/1361-6439/ac0e7f.

[16] D. Ahmed, A. Ozcelik, N. Bojanala, N. Nama, A. Upadhyay, Y. Chen, W. Hanna-Rose, T.J. Huang, Rotational manipulation of single cells and organisms using acoustic waves, Nat. Commun. 7 (2016) 11085, https://doi.org/10.1038/ncomms11085.

[17] A. Hashmi, G. Yu, M. Reilly-Collette, G. Heiman, J. Xu, Oscillating bubbles: a versatile tool for lab on a chip applications, Lab a Chip 12 (2012) 4216–4227, https://doi.org/10.1039/c2lc40424a.

[18] S. An, R. Ranaweera, L. Luo, Harnessing bubble behaviors for developing new analytical strategies, Analyst 145 (2020) 7782–7795, https://doi.org/10.1039/d0an01497d.

[19] Y. Li, X. Liu, Q. Huang, A.T. Ohta, T. Arai, Bubbles in microfluidics: an all-purpose tool for micromanipulation, Lab a Chip 21 (2021) 1016–1035, https://doi.org/10.1039/d0lc01173h.

[20] M.R. Rasouli, M. Tabrizian, An ultra-rapid acoustic micromixer for synthesis of organic nanoparticles, Lab a Chip 19 (2019) 3316–3325, https://doi.org/10.1039/c9lc00637k.

[21] A.J. Conde, I. Keraite, A.E. Ongaro, M. Kersaudy-Kerhoas, Versatile hybrid acoustic micromixer with demonstration of circulating cell-free DNA extraction from sub-ml plasma samples, Lab a Chip 20 (2020) 741–748, https://doi.org/10.1039/c9lc01130g.

[22] T. Yoshikawa, H. Kotera, K. Yoshida, D. Koyama, K. Nakamura, Y. Watanabe, Measurement of the resonant characteristics of a single bubble vibration by using a laser doppler vibrometer, Jpn. J. Appl. Phys. 50 (2011) 07HE04, https://doi.org/10.1143/jjap.50.07he04.

[23] T.F. Argo, P.S. Wilson, V. Palan, Measurement of the resonance frequency of single bubbles using a laser Doppler vibrometer, J. Acoust. Soc. Am. 123 (2008) EL121–EL125, https://doi.org/10.1121/1.2908195.

[24] S. Morioka, M. Ueda, K. Yoshida, D. Koyama, K. Nakamura, Y. Watanabe, Sound pressure threshold of non-spherical oscillation of an attached bubble evaluated by a laser Doppler vibrometer, in: 2012 Ieee International Ultrasonics Symposium 2012, pp. 767–770.

[25] J. Jeon, J. Hong, S.J. Lee, S.K. Chung, Acoustically excited oscillating bubble on a flexible structure and its energy-harvesting capability, Int. J. Precis. Eng. Manuf. Green Technol. 6 (2019) 531–537, https://doi.org/10.1007/s40684-019-00057-w.

[26] M. Guedra, C. Inserra, C. Mauger, B. Gilles, Experimental evidence of nonlinear mode coupling between spherical and nonspherical oscillations of microbubbles, Phys. Rev. E 94 (2016), 053115, https://doi.org/10.1103/PhysRevE.94.053115.

[27] T. Zhang, C. Guo, Z. Jiang, X. Wei, Internal resonance between the extensional and flexural modes in micromechanical resonators, J. Appl. Phys. 126 (2019) 537–540, https://doi.org/10.1063/1.5115028.

[28] G. Tang, B. Yang, C. Hou, G. Li, J. Liu, X. Chen, C. Yang, A piezoelectric micro generator worked at low frequency and high acceleration based on PZT and phosphor bronze bonding, Sci. Rep. 6 (2016) 38798, https://doi.org/10.1038/srep38798.

[29] C. Wang, B. Rallabandi, S. Hilgenfeldt, Frequency dependence and frequency control of microbubble streaming flows, Phys. Fluids 25 (2013), 022002, https://doi.org/10.1063/1.4790803.

[30] T. Zhang, P. Zhou, T. Simon, T. Cui, Ieee, A circular vibrating electrode with enhanced mass transfer for high-performance electrochemical sensors, in: 2021 34th Ieee International Conference on Micro Electro Mechanical Systems 2021, pp. 779–782.

[31] M.H. Abdel-Aziz, I. Nirdosh, G.H. Sedahmed, Mass and heat transfer behavior of oscillating helical coils in relation to heterogeneous reactor design, Aiche J. 63 (2017) 3141–3149, https://doi.org/10.1002/aic.15614.

[32] G. Batley, T.J.J.o.E.C. Florence, I. Electrochemistry, An evaluation and comparison of some techniques of anodic stripping voltammetry, 55 (1974) 23–43,

[33] M.G. Paneli, A. Voulgaropoulos, Applications of adsorptive stripping voltammetry in the determination of trace and ultratrace metals, Electroanalysis 5 (1993) 355–373, https://doi.org/10.1002/elan.1140050502.

[34] D. Grieshaber, R. MacKenzie, J. Vörös, E.J.S. Reimhult, Electrochemical biosensors-sensor principles and architectures, 8 (2008) 1400–1458.

[35] Y. Lu, X. Liang, C. Niyungeko, J. Zhou, J. Xu, G. Tian, A review of the identification and detection of heavy metal ions in the environment by voltammetry, Talanta 178 (2018) 324–338, https://doi.org/10.1016/j.talanta.2017.08.033.

[36] T. Zhang, Q. Liu, X. Wei, Z. Jiang, T. Cui, A vibrating membrane working electrode for highly sensitive anodic stripping voltammetry, Sens. Actuators B Chem. 311 (2020), 127948, https://doi.org/10.1016/j.snb.2020.127948.

[37] R. Venkatasubramanian, K. Jin, N.S. Pesika, Use of electrochemical deposition to create randomly rough surfaces and roughness gradients, Langmuir 27 (2011) 3261–3265, https://doi.org/10.1021/la200245m.

Tianyi Zhang was born in Qinhuangdao, Hebei, China in 1990. He received his B.S. and Ph.D. degrees from the Department of Mechanical Engineering at Xi'an Jiaotong University (Xi'an, Shanxi, China) in 2013 and 2019. He spent one year at the University of Minnesota as a visiting scholar. He is now a post-doctoral associate of the Department of Mechanical Engineering at the University of Minnesota. His research interests include vibration mode coupling in micromechanical resonators & oscillators and mass transport in electrochemical sensing applications.

Peng Zhou was born in Ningguo, Anhui, China in 1993. He received the B.S. in 2015 from the Department of Mechanical Engineering at Beijing Institute of Technology, China. Then he got M.S. degrees in mechanical engineering from the Purdue University Northwest, USA. He is currently a Ph.D. candidate student guided by Prof. Tianhong Cui in the Department of Mechanical Engineering in the University of Minnesota. His research interests include the photocatalytic water purification and MEMS based microsensors for both environmental and biomedical applications.

Terrence W. Simon received the B.S. degree in mechanical engineering from Washington State University, Pullman, WA, in 1968 and the M.S. degree in mechanical engineering from the University of California at Berkeley, Berkeley, CA, in 1971. He received the Ph.D. degree in mechanical engineering from Stanford University, Stanford, CA, in 1980. He is the Ernst G. Eckert Professor of the Department of Mechanical. His major research interests include experiments, computation and visualization of heat, mass and momentum transfer in laminar, turbulent, transitional and unsteady flows, including flows through porous media and processes with phase change. Applications range from flow and heat transfer in plasma cutting tools and plasma flow actuators, electronics and optics, Stirling and gas turbine engines, and MW-level grid energy storage systems. Dr. Simon is an active member of the American Society of Mechanical Engineers (including a past five-year term as the Senior Technical Editor of the Journal of Heat Transfer), the International Centre for Heat and Mass Transfer (in which he is now the President and has served on the Executive Committee), and the American Society of Thermal and Fluids Engineers (for which he co-chaired the International Workshop on Heat Transfer in 2017).

Tianhong Cui (SM'04) received the B.S. degree in mechanical engineering from Nanjing University of Aeronautics and Astronautics, Nanjing, Jiangsu, China, in 1991 and the Ph.D. degree in mechanical engineering from the Chinese Academy of Sciences, Changchun, Jilin, China, in 1995. He is currently a Distinguished McKnight University Professor at the University of Minnesota. From 1995–2003, he held research or faculty positions at Tsinghua University, University of Minnesota, National Laboratory of Metrology in Japan, and Louisiana Tech University. His current research interests include MEMS and nanotechnology. Dr. Cui is an Adjunct Professor at Mayo Clinic, a Distinguished Visiting Fellow at the University of Cambridge, and a Distinguished Visiting Professor at University of Paris-Est in France. He is a Fellow of American Society of Mechanical Engineering (ASME). He is the founding Executive Editor-in-Chief for two Nature journals, *Light: Science & Applications* and *Microsystems & Nanoengineering*. He is also serving as the founding Editor-in-Chief for the first AAAS/Science Partner Journal titled *Research*.